Journal Pre-proof

Structural, electronic and mechanical properties of all-sp^2 carbon allotropes with density lower than graphene

Tommaso Morresi, Andrea Pedrielli, Silvio a Beccara, Ruggero Gabbrielli, Nicola M. Pugno, Simone Taioli

PII: S0008-6223(19)31259-X

DOI: https://doi.org/10.1016/j.carbon.2019.12.024

Reference: CARBON 14874

To appear in: *Carbon*

Received Date: 26 August 2019

Revised Date: 30 November 2019

Accepted Date: 10 December 2019

Please cite this article as: T. Morresi, A. Pedrielli, S.a Beccara, R. Gabbrielli, N.M. Pugno, S. Taioli, Structural, electronic and mechanical properties of all-sp^2 carbon allotropes with density lower than graphene, *Carbon* (2020), doi: https://doi.org/10.1016/j.carbon.2019.12.024.

Structural, Electronic and Mechanical Properties of all-sp^2 Carbon Allotropes with Density Lower Than Graphene

Tommaso Morresi[a, b], Andrea Pedrielli[a, b], Silvio a Beccara[a], Ruggero Gabbrielli[a], Nicola M. Pugno[b, c, d,*], Simone Taioli[a,*]

[a]*European Centre for Theoretical Studies in Nuclear Physics and Related Areas (ECT*-FBK) and Trento Institute for Fundamental Physics and Applications (TIFPA-INFN), Trento, Italy*

[b]*Laboratory of Bio-Inspired and Graphene Nanomechanics - Department of Civil, Environmental and Mechanical Engineering, University of Trento, Italy*

[c]*School of Engineering and Materials Science, Materials Research Institute, Queen Mary University of London, UK*

[d]*Ket Lab, Edoardo Amaldi Foundation, Italy*

[*]Corresponding author

[**]Corresponding author

Email addresses: nicola.pugno@unitn.it (Nicola M. Pugno), taioli@ectstar.eu (Simone Taioli)

Abstract

In this work we propose a few novel energetically and dynamically stable all-sp^2 carbon-based architectures with low density obtained by augmenting planar three-coordinated uniform tessellations. Using geometrical packing arguments, we show that such arrangements satisfy the locally–jammed packing condition and represent some of the least dense structures of all-sp^2 bonded carbon allotropes that could ever be synthesized. We fully characterize from first principles these new architectures, by assessing i) the electronic properties, such as the band structure and the density of states; ii) the dynamical characteristics, such as the phonon dispersion; and iii) the mechanical properties, such as the elastic constants and the stress–strain relationships. We compare our findings with already synthesised carbon-based materials, in particular graphene, and we find that in the lowest–density structures the mechanical rigidity is considerably depleted, while other specific mechanical characteristics, such as toughness and strength, are comparable to the relevant specific values of graphene.

Keywords: graphene allotropes with low density, augmentation, density functional theory, electronic and mechanical properties, stress-strain curves

1. Introduction

Over the last decade graphene is arguably one of the most investigated materials among all the existing carbon allotropes [1, 2]. Indeed, despite the difficulties in synthesising high-quality large-area graphene sheets [3, 4, 5], its great promises and achievements in the fields of microelectronics, of materials science and chemistry motivate the great deal of scientific and technological efforts that scientists are pursuing.

Further progress in the search of potential applications of graphene to various materials and devices is mainly related to its unique electronic and mechanical properties [6, 7, 8, 9, 10, 11, 12, 13, 14, 15], even though the quest for practical applications have shifted the focus over the years to other layered materials, such as transition-metal dichalcogenides (TMDs) [16], silicene [17], germanene, the monolayer form of black phosphorous [18, 19], and boron-nitride. Moreover, the power of modern supercomputer platforms, novel algorithms [20] and approaches e.g. based on artificial intelligence [21] have paved the way also to the discovery of several other layered hybrid materials [22] with the aim of combining together the most desirable characteristics of each layered structure [11, 23], starting a specific research field on 2D materials.

Nevertheless, the possibility to introduce new interesting features also in bi-dimensional carbon-based materials without chemical functionalization, while keeping the desirable properties of graphene, such as its planar periodic structure and the sp^2 bonding network, might be very convenient to the existing technology. One parameter that can be modified e.g. is the atomic density, which could be in principle

lowered to obtain lightweight, strong graphene allotropes. In this regard, one of the most striking properties of graphene is its Young's modulus to density ratio, probably the highest achieved so far. Thus, one may devise a route to design novel carbon-based materials with a density lower than graphene, while keeping its specific properties. Unfortunately, investigations on this topic have been rarely pursued except for some notable exceptions [24, 25, 26, 27].

In this work, using an augmentation method applied to regular and semi-regular tessellations of the plane with three-connected vertices, we find some novel energetically stable sp^2-bonded carbon-based structures under the locally jammed packing condition with density lower than graphene. Our ultimate goal is to decrease the surface density possibly up to the least dense form of sp^2-carbon allotrope that could ever be synthesized, while displaying almost unchanged specific mechanical characteristics with respect to graphene. Indeed, one of the possible routes to increase the specific modulus with respect to graphene can be achieved via reducing the surface density. Increasing the specific modulus by decreasing the mass density is a typical request whereby the minimum structural weight can be achieved. This challenge has far-reaching consequences in a variety of applications, most notably in aerospace technologies where weight saving is a route to cost reduction.

Furthermore we show that the same augmentation procedure can be extended to a larger class of planar tessellations, including for example the Cairo tiling. The stability of parent and augmented (daughter) carbon structures created via this augmentation approach is probed by calculating the phonon dispersion from first principles as well as ab-initio molecular dynamics (AIMD).

Finally, their response to external deformation and electromagnetic fields is probed by assessing the stress–strain curves, including their specific mechanical properties, and the electronic band structures. In the latter case in particular we find that the augmentation procedure leads to a lower density but also to frustrated geometries with characteristics flat bands around the Fermi level, therefore enabling the creation of realistic strongly-correlated materials. From the mechanical point of view, we observe that the mechanical rigidity is very much depleted by decreasing the density, while other specific mechanical characteristics, such as the strength and toughness, can be even bigger than graphene.

2. Methods and computational details

2.1. The augmentation procedure

To generate graphene allotropic structures we devise and implement an algorithm based on the augmentation of regular and semi-regular tessellations of the plane with three-connected vertices. These tessellations can be also represented by the two-dimensional packing of congruent discs under the conditions that i) each disc must be in contact with at least another disc without overlap, ii) there exists a path connecting the discs through mutual contacts. To restrict the possible structural search of planar carbon architectures we also require that i) the atomic centers are three-coordinated, ii) the maximum angle between two bonds is below π rad, and iii) the structures are periodic. The choice of angles lower than π rad corresponds to the so-called locally jammed (or stable) packing and prevents the notable increase of angle strain in sp^2 carbon allotropes far from equilibrium configuration. For locally stable disc packing, contacts between circles should not lie all on the same hemicircle [28]. With such a constraint in place, one might wonder whether packings of arbitrarily low density exist or, in case they do not, what the least dense arrangement of discs in the plane would be. It is an interesting question on its own, given that the question addressing the opposite problem – that of finding the densest arrangement of discs in the plane – received much attention for a long time [29, 30] and found a formal answer only in the last century [31]. In this regard, it is worth noticing that if the packing is allowed to be non-periodic, then discs can indeed be packed into locally stable configurations with arbitrarily low density [32].

Under the local stability conditions, we achieve a decrease of the structural density by substituting every vertex of the parent carbon net with three atomic centers arranged in an equilateral triangle. In this way we are able to produce carbon-based daughter architectures that are still three-coordinated; furthermore, this procedure can be in principle repeated until reaching all triangular nodes as well as generalized beyond regular and semi-regular tessellations, e.g. to the case of the Cairo pentagonal tiling in which two vertices of the unit cell are four-coordinated. Below we will show the application

of our augmentation method to both well-established and novel carbon materials. More details on the augmentation procedure can be found in the Supplementary Information.

2.2. Structure optimization

The optimization of the atomic positions and unit cells, electronic and phonon band structure simulations, as well as the assessment of the mechanical properties of the proposed architectures were performed within the DFT framework using the QUANTUM ESPRESSO (QE) suite [33]. QE is a plane-wave code based on the pseudopotential approach to deal with the interaction between valence electrons and lattice ions.

Optimization of the atomic configurations was carried out by using Broyden–Fletcher–Goldfarb–Shannon (BFGS) algorithm. The simulation cells in the direction orthogonal to the plane of the structures was set to 20 Å, in order to avoid spurious interactions among periodic images. The forces between the atoms in the calculation supercells have been minimized below 0.01 eV/Å, which ensures convergence of the structural parameters of graphene to better than 0.05%. The optimized configurations along with the supercell sizes of all graphene allotropes are reported in the supplementary material.

The carbon structure optimization has been performed using different exchange and correlation (XC) potentials respectively for the phonon dispersion calculations, where we adopted the Local Density approximation (LDA), and for the band structure simulations, where we adopted the PBE XC. The former choice was imposed for avoiding the presence of negative frequencies, which are known to appear more likely with finite cut-offs using GGA functionals, which have functional forms more strongly varying with the position. The use of PBE functionals is at variance suggested for electronic structure simulations of carbon-based materials.

2.3. Phonon band structure simulations

To assess the stability of the parent and daughter structures we computed the phonon bands using the *ph.x* utility of QE. We used the LDA ultrasoft pseudopotential *C.pz-rrkjus.UPF* [33], with a cut–off of 30 Ry for wavefunctions and 240 Ry for the density, respectively. These cut-off values were set-up after achieving a well-converged phonon band structure of graphene in comparison to experiments and previous simulations. The *k*-point grid used to carry out phonon calculations was chosen so to obtain converged DFT values below chemical accuracy ($<$ 0.01 eV for the total energy and $<10^{-3}$ Ry/Å for the interatomic forces). Depending on the simulation cell dimensions, we performed calculations on $2\times2\times1$ up to $16\times16\times1$ *k*-point grids for structural optimization, while increasing the *k*-point mesh to $48\times48\times1$ for the calculation of the band structures. Convergence of the integrals over the Brillouin zone was improved by smearing the occupancy with a 0.136 eV width Gaussian function. Simulation cells were carefully relaxed to achieve the minimum-energy configurations with respect to this pseudopotential. The convergence threshold for the self-consistent electronic structure simulations was set to 10^{-14} Ry and to 10^{-17} Ry for the phonon calculations. These small values of the thresholds were necessary to avoid the appearance of spurious imaginary frequencies not due to instabilities of the structural arrangement.

2.4. Electronic band structure and DOS

To carry out DFT electronic band structure simulations we used a norm conserving PBE pseudopotential (*C.pbe-mt_gipaw.UPF*) and an energy cut-off for the wavefuntions equal to 100 Ry. This large value of the plane-wave cut-off is due to obtaining converged values of the stress tensor, an observable notoriously more difficult to converge with respect to the total energy. The electronic free energy of the primitive cells was converged to within less than 0.1 meV. The *k*-point grids used to calculate observables in the momentum space are the same than those used in phonon band structure calculations.

2.5. Mechanical properties

The mechanical properties were assessed by using the same parameters of the electronic band structure simulations (see section 2.4). For carrying out the calculation of the mechanical properties in

linear regime we used 0.001-spaced points up to 0.01 strain and further 0.005-spaced points up to 0.05 strain. To deal with the elastic deformations we used supercells containing two unit cells for the materials with trigonal symmetry, i.e. the graphene and the flakene families. The C_{11} coefficient in these cases is related to the strain along the zigzag direction. Upon deformation, the atomic positions within the supercell were relaxed until interatomic forces were smaller than 10^{-3} Ry/Å. In this regard, we stress that in our ab-initio simulations we assess thus the "*true stress*", so the simulation supercell is allowed to change in the direction orthogonal to the loading to obtain atomic forces below 0.5 kbar, equivalent to $0.5 \times 20 / 3.35 = 3$ kbar. The stress–strain characteristics of graphene allotropes are reported by choosing a conventional thickness equal to the interplanar distance in graphite, namely 3.35 Å. This thickness is the value used in the manuscript for all the structures.

3. Results and discussion

The carbon-based sp^2 structures analysed in this work are reported in Fig. 1. In particular in the panels from *(a)* to *(h)* of this figure, we present in red what we call the parent geometries (that are already known systems in literature), while in blue the augmented-daughter structures. In the panels *(i)* and *(l)* we show that by relaxing the locally jammed packing condition, an arbitrarily low density sp^2 material can be designed. We notice that to the best of our knowledge *tilene, flakene, liskene* and *liskene daughter* are novel architectures. Nevertheless, to compare the properties of these daughter structures with the relevant parent nets we present also the structural arrangements and the assessment of the electronic and mechanical properties of the latter, despite they represent well established architectures [34, 35, 36].

Figure 1: First row: in the upper panel parent (left, red color) and daughter (right, blue color) disc packing in the unit cells of a) graphene, c) tilene, and e) flakene. The lines internal to the discs connect the nearest neighbors. Bottom panel of the first row: 4×4 supercells of parent (left) and daughter (right) structures of b) graphene, d) tilene, and f) flakene. Second row: g) from left to right: pentagraphene structure; augmentation of the Cairo pentagonal tiling: liskene; further augmentation of the liskene geometry: liskene daughter. h) from left to right: top and side view of a 3×3 pentagraphene supercell, where the sp^3-hybridized carbon atoms are reported in green color, while in grey we find the sp^2-hybridized carbon centers; 3×3 supercell of liskene and liskene daughter after performing DFT minimization. i) By relaxing the locally jammed packing constraint, the flakene structure can be made progressively less dense by elongating the hexagonal super-ring side highlighted in the picture. l) The low density structure obtained from flakene by doubling the hexagonal super-ring side length.

3.1. Structural optimization

Table 1: First column: structure type. Second column: surface density. Third and fourth columns report the total energy per atom with respect to graphene and the cohesive energy per atom obtained upon structural optimization, respectively. With the exception of pentagraphene, all structures are planar and each carbon atom is three-coordinated. In the table the following abbreviations were used: p.=parent, d.=daughter, dir.=direct gap, indir.=indirect gap.

Structure	Density	Energy	Cohesive energy	Type	Bandgap
	(atoms/Å^2)	([eV]/atom)	([eV]/atom)		[eV]
Graphene	0.379	0	7.7404	Semi-met.	0 (dir.)
Graphene d.	0.256	0.9882	6.7523	Metal	-
Tilene p.	0.336	0.5186	7.2219	Metal	-
Tilene	0.233	1.0765	6.6640	Metal	-
Flakene p.	0.301	0.6395	7.1009	Semi-met.	0.043 (dir.)

Flakene	0.212	1.1071	6.6334	Metal	-
Pentagraphene	0.452	0.9044	6.8361	Semicond	2.23 (indir.)
Liskene	0.297	0.7789	6.9615	Semicond	0.36 (indir.)
Liskene d.	0.247	1.0506	6.6897	Semicond	0.46 (indir.)

Prior performing the analysis of the mechanical and electronic properties of the proposed carbon nets, we carry out the structural optimization (see section 2 for the DFT parameters used).
In the third and fourth columns of Table 1 we report the energy and the cohesive energy per atom after optimization of the atomic positions within the cell for all structures. The cohesive energy of graphene (7.74 eV) well agrees with the experimental value of 7.6 eV [37], and with previous DFT simulations [38] reporting a value of 7.828 eV. We notice that graphene is still the most energetically stable allotrope.
In general, with the notable exception of pentagraphene, we observe that lowering the densities of the parent structures by using the previously introduced augmentation method results in daughter architectures characterized by lesser energetic stability and lower intra-molecular bond strengths. We rationalize the different finding in the case of pentagraphene, for which the cohesive energy increases from parent to daughter, by noticing that the augmentation starts from a non-planar $sp^2 - sp^3$ net and ends up into a purely planar sp^2 net. This atomic arrangement represents thus a favourable solution from both the energetic and density points of view.
For the flakene parent we find almost the same energy difference (0.6395 eV vs. 0.64 eV) with respect to graphene (see third column of table 1) as in [39], where this structure is labelled "graphenylene". Also for the tilene parent we calculate an energy difference with respect to graphene equal to 0.5186 eV, which is very similar to the value of 0.53 eV reported in [24], where the structure was named T-graphene. Finally, in the case of pentagraphene we find an energy-per-atom difference of 0.904 eV, which is very much comparable to the value of about 0.9 eV reported in [40].
While we notice that the loss of stability is not significant, as the total energy difference per atom between the less stable material (flakene) and graphene is of the order of 1%, the density is almost two times lower than that one of graphene (see the second column of table 1).

3.2. Phonon band structures and thermodynamic stability of graphene allotropes with lower density

To test the dynamical stability of the novel structures proposed in this work we computed the phonon dispersion curves. The phonon band structures, calculated with the parameters described in section 2.3, are reported in figure 2 for the parent and the daughter structures, respectively. The high-symmetry points in momentum space that have been selected to represent the phonon bands in systems characterised by hexagonal lattice are Γ: (0,0), M: (1/2,0), K: (2/3,1/3). The high-symmetry lines in the Brillouin zone connect the points $\Gamma - M - K - \Gamma$ to form a triangle in momentum space. In systems characterised by simple square lattice the phonon bands are at variance represented by the high-symmetry points Γ: (0,0), M: (1/2,1/2), X: (1/2,0). The high-symmetry lines in the Brillouin zone connect the points $\Gamma - X - M - \Gamma$ to form a triangle in momentum space. In Fig. 2 we report also the typical labels of the graphene phonon bands that are the TO, LO and LA branches, which can also be found in the other structural configurations.
In general, good agreement between our calculations and experiment [41] for the TO, LO and LA branches of graphene is found. This shows the accuracy of the basis set and density functional parameters used in this work. The small splitting of the LO and LA phonons at the M point equal to 22 cm^{-1} well compares with the experimental value of 35 cm^{-1} reported by inelastic X-ray scattering [41]; the splitting between the TO and LA modes at the K point equal to 93 cm^{-1} resembles the experimental value of 71 cm^{-1}, closer with respect to other theoretical simulations, which reported a value of 120 cm^{-1} [42] and 140 cm^{-1} [43], respectively. The zone center phonon value 1577 cm^{-1} is slightly below the experimental values for graphite and graphene (1582 cm^{-1}) measured recently [4, 44]. These differences can be explained by taking into account that other

authors have estimated uncertainties of 10 cm^{-1} for the frequencies higher than 1300 cm^{-1} [45, 46]. In particular, we notice that all the proposed new systems are dynamically stable as we could not find negative frequencies along the momentum axis. This definitely means also that our structures are accurately optimized.
Moreover, in the daughter architectures we notice the emergence of a phononic gap, which is not present in the parent structures, in the energy range 800–1200 cm^{-1}. In this energy range the phonon bands show an almost flat behaviour. These modes arise owing to the presence of triangular shapes in the daughter architectures and are characterized by very small group velocities. Similar findings are reported in Ref. [47], where the authors studied the propagation of elastic waves in 2D hierarchical hexagonal lattice structures. The emergence of phonon band gaps in the daughter structures above 800 cm^{-1} is also reported in Ref. [48], where the insertion of micro-structures within the unit cell, such as triangular shapes, could be used to prevent the propagation of mechanical waves in this frequency range.

Figure 2: Phonon band structures of the parent (left panel, red lines) and daughter (right panel, blue lines) architectures of a) graphene, b) tilene, c) flakene, and d) pentagraphene.

In order to verify the thermodynamic stability of our structures we also carried out ab initio molecular dynamics (AIMD) simulations at 500 K lasting 10 ps. The results show that all our structures are thermodynamically stable with no phase transition observed. Diffusion coefficients were found to be below 0.03 mm^2/s, which substantiates our structure generation approach. A movie reporting the AIMD trajectory simulations in the case of tilene has been uploaded as supplemental information.

3.3. Electronic properties

Figure 3: Upper panels: band structure of the parent (left, red lines) and daughter (right, blue lines) architectures of a) graphene, b) tilene, c) flakene, and d) pentagraphene. Lower panels: relevant DOS of the parent (red filled area) and daughter (blue filled area) structures. Fermi level is shifted to zero and reported as an horizontal (vertical) green line in the band structure (DOS) plots.

In this section we report the band structures and DOSs for all the structural arrangements investigated in this work.
We begin with the well known electronic band structure of graphene reported in the upper left panel of figure 3(a) alongside the DOS (red filled curve in the lower panel of figure 3(a)), which we reproduce to test our choice of the DFT parameters. The agreement with previous simulations [49] is excellent so we can move to the assessment of the electronic structure of the other systems.
In the right panel of figure 3(a) we report the bands of the graphene daughter. We observe that graphene loses its semi-metal characteristics and acquires a striking metallic behaviour with a loss of the typical graphene features near the Fermi energy (valence and conduction bands do not touch in Dirac points as well as the dispersion around the Γ-point is not linear). This is due to the appearance of a narrow band close to the Fermi level (reported as an horizontal (vertical) green line in the band structure (DOS)), a feature that appears also in tilene and flakene, as can be seen in the upper right panels of figures 3(b) and 3(c). This is of course reflected into the DOS, characterized by a narrow peak close to the Fermi energy, as shown in the blue filled curves reported in the lower panels of figure 3(a), 3(b), and 3(c).
Tilene parent and flakene parent electronic band structures (see upper left panels in figures 3(b) and 3(c), respectively) are not dramatically changed by augmentation, as the daughter structures stay metallic (see lower panel in figure 3(b) for tilene daughter) or increase their metallic character (see lower panel of figure 3(c) for flakene daughter).
At odds with the previous architectures, pentagraphene band structure (see upper left panel of figure 3(d)), which has the typical characteristics of a semiconductor (in agreement with previous DFT calculations [40]), is heavily affected by augmentation, as the daughter structure (see upper right panel of figure 3(d)) presents an almost semi-metallic behaviour characterized by a very narrow band gap. The relevant DOSs of pentagraphene (filled red curve of figure 3(d)) and liskene (filled blue curve of figure 3(d)) are typical of a semiconductor and semi-metal, respectively.

The presence of an almost flat band (FB) around the Fermi energy in the daughter structures can be rationalized by using a Tight Binding (TB) approach. In such FBs, the kinetic energy of electrons is quenched in favour of the enhancement of their Coulomb interaction.

Figure 4: a) Kagome lattice (left panel) and TB calculations of the band structure using an hopping parameter $t = 1$ (right panel). b) The graphene daughter lattice and the relevant TB electronic structure simulations using an hopping parameter $t = 1$. In both cases we perform the simulations by including only the p_z orbital.

We argue that the appearance of a FB in the band structure of our daughter architectures can be attributed to the electronic orbital frustration, similarly to the Kagome lattice, reported in Fig. 4(a), left panel. The Kagome lattice [50, 51] is composed of interlaced triangles in which each lattice point interconnects two neighboring hexagons. This geometry is very similar to the graphene daughter architecture, where at variance each unit cell contains six carbon atoms, which form two separate equilateral triangles symmetrically placed with respect to an inversion center at the center of the unit cell (see Fig. 4(b), left panel).
The origin of FBs in the Kagome lattice has been explained in terms of destructive interference between nearest neighbors, which results in localized eigenstates of the Hamiltonian [51]. Indeed, the wavefunction amplitude alternates its sign around the six vertices (see Fig. 4(a), left panel). Consequently, electrons are trapped within the hexagon as net hoppings originating from the two adjacent vertices cancel each other [52], and a FB appears (see Fig. 4(a), right panel). In these TB simulations we include one p_z orbital for each carbon atom, due to the planar geometry of the Kagome lattice, and we project the DOS over this manifold. We interpret the existence of FBs in the electronic structures of our graphene allotropes as due to the same frustration effect of the orbitals in the lattice. In particular, in Fig. 4(b), right panel, we report the TB simulations of the graphene daughter electronic band structure. Notice that the only exception to this rule is liskene, where the presence of square polygons spoils the orbital frustration and favours electron delocalization. Nevertheless, liskene daughter geometry restores triangular shapes via our augmentation procedure and, thus, a FB reappears.

3.4. Elastic properties

To characterize the mechanical properties of the daughter architectures in comparison to the parent structures we carried out first the ab-initio simulations of the elastic stiffness tensor $\mathbf{C}$. The matrix $\mathbf{C}$ provides in linear approximation the proportionality or elastic constants relating the stress and the strain, $\boldsymbol{\sigma} = \boldsymbol{\varepsilon}\mathbf{C}$ where $\boldsymbol{\varepsilon}$ is the six-component strain vector, and $\boldsymbol{\sigma}$ is the stress tensor. The stiffness tensor is in principle characterized by six independent terms in bi-dimensional materials, being $C_{ij} = C_{ji}$ for symmetry considerations. The elastic behavior of orthotropic 2D materials can be described thus by four elastic constants C_{11}, C_{22}, C_{12} and C_{44} [53]. For the square lattice structures, such as tilene parent, tilene and liskene, the symmetry constraint sets $C_{11} = C_{22}$, so that one has only three independent elastic constants. Graphene, graphene daughter, flakene parent and flakene at variance show isotropic hexagonal symmetry, reducing the independent elastic constants to only two according to the relations $C_{11} = C_{22}$ and $2C_{44} = C_{11} - C_{12}$.
In harmonic approximation, so for small displacement, the strain–energy density function *F* at 0 K can be expressed as

$$F = F_0 + \frac{1}{2}F^{(2)}\varepsilon^2 + o\left(\varepsilon^3\right) \qquad (1)$$

where F_0 and $1/2F^{(2)}\varepsilon^2$ are the static energy of the system and the vibrational contribution of the lattice, respectively. In our simulations we neglect the thermal electronic contribution, which is expected to be low.
The elastic constants C_{ij} can be then expressed as follows:

$$C_{ij} = \frac{\partial^2 F}{\partial \varepsilon_i \partial \varepsilon_j} \quad (2)$$

Table 2: Elastic constants (C_{11}, C_{12}, C_{44}), area Young's modulus (E_A), Young's modulus (E), Poisson's ratio (v) and area specific Young's modulus (E_A / ρ_A) of the parent and daughter carbon structures. To evaluate the accuracy of our simulations, we report a comparison with data in the literature where available. In the table the following abbreviations were used: p.=parent, d.=daughter.

	C_{11}	C_{12}	C_{44}	E_A	E	v	E_A / ρ_A
	(N/m)	(N/m)	(N/m)	(N/m)	(TPa)		(10^{-3} Nm kg $^{-1}$)
Graphene	348	53.8	-	340	1.015	0.154	1.79
[34]	358	60	-	349		0.17	
Graphene d.	149	94.0	-	89.6	0.267	0.631	0.70
[34]	152	98	-	92.6		0.64	
Tilene p.	294	44.1	48.3	288	0.860	0.150	1.70
[54]	296	46	49	306		0.13	
Tilene	124	75.5	11.3	78.6	0.235	0.607	0.67
Flakene p.	220	57.7	-	205	0.612	0.263	1.36
[34]	227	61	-	210		0.27	
Flakene	87.0	64.9	-	38.6	0.115	0.746	0.36
Liskene	187	94.8	52.0	138	0.412	0.508	0.93
Liskene d.	127	65.6	19.4	93.1	0.278	0.517	0.75

The C_{ij} s can be derived by fitting the energy density of equation 1 with a second order polynomial in the imposed strain.

In particular, on the one side for isotropic materials the fitting parameter $F^{(2)}$ can be identified with C_{11} for uniaxial deformation and with $2(C_{11}+C_{12})$ under hydrostatic deformation, respectively. On the other side, in the case of orthotropic materials further calculations are needed in order to fully characterize the stiffness matrix. In this case, the elastic constants C_{11}, C_{22} can be identified as the fitting parameters of the total energy under uniaxial strain, while $F^{(2)}$ corresponds to $C_{11}+C_{22}+2C_{12}$ or $4C_{44}$ in the case of hydrostatic deformation or shear deformation, respectively. From the knowledge of the elastic constants, the Young's modulus *E*, which measures material stiffness, and the Poisson's ratio *v*, which measures the material tendency to expand in directions perpendicular to the direction of compression, can be computed as $E = \left(C_{11}^2 - C_{12}^2\right)/C_{11}$ and $\nu = C_{12}/C_{11}$, respectively.

Figure 5: Biaxial elastic modulus versus area density. The inset reports the linear fit of the absolute biaxial modulus from our simulations of graphene allotropes (black line) along with that of Ref. [34] (dashed line). In the larger graphic the linear fit has been divided by the surface area to obtain the specific biaxial modulus; the grey dashed line shows the data of Ref. [34], while the black curve report our simulated data.

In table 2 we report the elastic constants, Young's modulus and Poisson's ratio of all the 2D carbon allotropes studied in this work in comparison with the DFT values reported in the literature [34, 54], finding a remarkable agreement with previous available calculations and experiments. We remind that, at variance with a stable, isotropic, linear elastic 3D material where the bounds on Poisson's ratio are $-1<\nu<1/2$, for 2D materials one has $-1<\nu<1$ [55]. Therefore, it is not surprising to obtain values of the Poisson's ratios higher than 1/2 for our 2D architectures.

The Young's modulus of graphene obtained from our DFT simulations is in good agreement with the experimental value of 1 ± 0.1 TPa (assuming a graphene thickness equal to 0.335 nm), obtained by nanoindentation measurements on single-layer graphene [56]. The analysis of the Poisson's ratio of tilene, flakene and liskene shows that these materials are almost incompressible. More precisely, the Poisson's ratio of tilene (as of graphene daughter, flakene, and liskene) is higher than the limit of isotropic incompressible 3D materials (which is 0.5) while lower than the corresponding upper bound on Poisson's ratio for 2D materials (which is 1 [55]): this material presents a hyper-restriction correspondent to a decrease of the area under tension.

Tilene presents an area Young's modulus $E_A = 78.6$ N/m and a Poisson's ratio $\nu = 0.607$, which are similar to those of the graphene daughter. Flakene has an area Young's modulus $E_A = 38.6$ N/m and a Poisson's ratio $\nu = 0.746$. Generally, we notice that graphene has the highest Young's modulus, and that moving from parent to daughter structures the Young's modulus decreases and the Poisson's ratio consequently increases.

Moreover, one of the most significant observables to be computed for low density materials is of course the specific modulus, namely the Young's modulus divided by the mass density. Thus, we computed the Young's modulus per mass density $E_A/\rho_A = E/\rho$, where ρ_A is the density in units of Kg/m^2 and ρ the mass density in Kg/m^3. The outcome of our simulations concerning this quantity are reported in the last column of table 2. We notice that graphene presents the highest specific modulus among the materials studied here. At odds flakene, while displaying the lowest density among the investigated structures, shows a major drop in both the absolute and specific elastic moduli, which are from 8 to 5 times lower than graphene. Nevertheless, while we do not find a material outperforming the specific properties of graphene in this respect and, thus, we do observe that the augmentation is only partially an advantageous route to follow in order to increase the specific modulus of graphene-like materials, the difference in the specific Young's modulus is less remarkable than for the absolute values, with the exception of flakene.

The drop of flakene Young's modulus suggests that there is a threshold to the decrease of the density of these carbon-based planar materials, below which this mechanical characteristic is significantly depleted. In order to get further insights on this issue, we report in figure 5 the specific modulus of our carbon allotropes versus area density. In particular, we plot the specific biaxial modulus ($E_{bi} = C_{11} + C_{12}$) versus the area density, in comparison to the fit of the data reported in [34] by the formula $E_{bi} = 1184.3 \times \rho_A - 56.88$ (N/m)/(atoms/Å^2) (gray dashed curve in figure 5). Notice that the gray dashed line in figure 5 represents a fit of the specific (and not of the absolute) biaxial modulus vs. density for several graphene allotropes. We stress that the non-linear behaviour concerns thus the specific and not absolute quantities. In the inset of figure 5 we report indeed the untouched data provided in Ref. [34] referred to the absolute biaxial modulus vs. density for the graphene allotropes therein investigated. In this case the fit of our data is closer to a straight line ($E_{bi} = 1445.7 \times \rho_A - 147.78$ with an R^2 value exceeding 0.965) and is similar to that provided in Ref. [34]. It is worth to notice that in Ref. [34] the authors analyse also sp-sp^2 2D carbon–based structures, in this way further lowering the density. Here at variance, we only consider sp^2–connected architectures. This feature explains the small difference between the two angular coefficients of the linear fits of the absolute biaxial modulus reported in the inset of figure 5.

Our findings clearly point towards the existence of a correlation between density and biaxial modulus; nevertheless, we notice that density cannot be the only factor that in principle affects the mechanical properties. Additionally, we point out that for flakene a clear depletion of this mechanical characteristic is found, meaning that the density decrease does not compensate the loss of mechanical

stiffness. These findings led us to the conclusion that the idea of decreasing the density, retaining the specific mechanical characteristics, can be pursued only to some extent at least as far as the Young's modulus is concerned.

3.5. Stress–strain curves

Figure 6: Stress–strain curves of graphene and graphene daughter along the *x*-direction (or zigzag, represented by red and blue empty squares for the two architectures, respectively) and the *y*-direction (or armchair, represented by green and violet empty circles for the two architectures, respectively). The differently colored lines represent only a guideline for the eye. Experimental data from Ref. [56, 57]

To gain further insight on the dependence of the mechanical properties of our structures on the density, we carried out the first-principles simulations of the stress–strain curves from which several observables can be obtained, such as the fracture strain, the tensile strength and the toughness. DFT calculations of the true stress tensor in response to strain, from which one can develop constitutive equations to fit the ab-initio data, were performed on the unit cell of the materials. We remind that all structures were relaxed below 3 kbar in the direction orthogonal to loading, and we plot the stress obtained by using the relaxed surface (true stress as opposed to engineering stress).
In figure 6 we start from analyzing the stress–strain curves of graphene and graphene daughter to benchmark our results against the extensive number of computational and experimental (reported as crosses in Fig. 6) studies carried out in this respect, along the Cartesian directions x, y, which represent the zigzag and armchair directions of graphene (or, better to say, of the zigzag and armchair ribbon that can be obtained by cleaving along the x, y directions), respectively. The stress–strain characteristics under uniaxial tensile loading along the zigzag (*x*, empty red squares) and armchair (*y*, empty green circles) directions, reported in figure 6, show the known anisotropic response of graphene that results in nonlinear constitutive equations [58, 59]. The lines connecting the calculated points of the stress-strain characteristics of all structures only work as a guideline for the eye.
The mechanical response of graphene to uniaxial tension is almost linear until about 10% strain for both the armchair and zigzag directions, with the curve slope progressively decreasing with increasing strain. Beyond that value the stress–strain curves deviate significantly from linearity, keeping the isotropic behaviour up to 15% strain, where the mechanical characteristics along the two loading directions fork. The anisotropy develops at rather moderate strain with the zigzag stiffness dramatically decreasing with respect to the armchair direction. In figure 6 we sketch also the mechanical response to loading along the *x* (empty blue squares) and *y* (empty violet circles) directions of the graphene daughter. We notice that the absolute mechanical properties deplete significantly from graphene to its daughter in all respect, with a strong decrement in toughness and strengths (see also table 3, where we report the absolute mechanical characteristics of these structures along with those of the other novel 2D architectures proposed in this work, that is tilene, flakene and liskene).

Figure 7: Stress–strain curves of tilene parent and tilene along the *x*-direction (red and blue empty squares for the two architectures, respectively) and the 45°-direction (green and violet empty triangles for the two architectures, respectively). The differently colored lines represent only a guideline for the eye. On the left and right sides of the image we report the simulation cells of tilene for different strain values and directions.

In this respect, we notice that the architecture of the graphene daughter is largely dominated by the presence of triangular shapes, at variance with graphene (see figure 1(b)). This feature is shared also by tilene (see figure 1(d)). This seems the major reason of the similar mechanical response to uniaxial strain along the *x*-direction between the graphene daughter (see violet empty circles in figure 6) and tilene (see blue empty squares in figure 7 for a comparison). Along the *y* direction the mechanical response of graphene daughter is similar to graphene (see violet empty circles in figure 6), showing a high fracture strain at lower stress than graphene.

Figure 8: Stress–strain curves of flakene parent and flakene along the *x*-direction (red and blue empty squares for the two architectures, respectively) and the *y*-direction (green and violet empty circles for the two architectures, respectively). The differently colored lines represent only a guideline for the eye. On the left and right sides of the image we report the simulation cells of flakene for different strain values and directions.

Figure 9: Stress–strain curves of liskene and liskene daughter along the *x*-direction (red and blue empty squares for the two architectures, respectively) and the 45°-direction (green and violet empty circles for the two architectures, respectively). The differently colored lines represent only a guideline for the eye.

Tilene parent and tilene (see figure 1(d)) belong to the dihedral group of symmetries (D4) and, thus, in figure 7 we reproduced the stress–strain characteristics along the *x* (empty squares, a strain along the *y* direction would provide the same results) and the diagonal (45°, empty triangles) directions. Tilene parent displays a behavior under mechanical loading similar to graphene along the *x*-direction (empty red square in figure 7) with comparable strength and proportional limit stress (see table 3). However, in the diagonal direction (see empty green triangles in figure 7) the presence of sp^2-carbon squares reduces the absolute mechanical performances of the tilene parent, but with a significantly higher fracture point (see table 3). Nevertheless, the stress–strain characteristics do not overlap along the two different directions. Tilene shows a mechanical response to uniaxial strain comparable to graphene daughter in both the *x* (blue empty squares of figure 7) and diagonal directions (violet empty triangles of figure 7), being its structure characterized by a similar occurrence of sp^2 triangles.
We notice that the data points in the stress-strain curves beyond the ultimate tensile strength (UTS) correspond to a bounce in stress due to structural modifications. However, while these points reveal that a phase transition occurs in our simulations, we point out that the calculations are performed using alternatively deformation and optimization steps. This procedure completely excludes dynamical effects such as heating due to the release of elastic energy or thermal fluctuations. The points beyond UTS in the stress-strain curves only emphasise the need of further studies aimed to investigate these possible structural transformations in the framework of molecular dynamics.

Figure 10: Comparison between the stress–strain curves of liskene, tilene, and flakene along the *x*-direction (blue, red and cyan empty squares for the three architectures, respectively), along the 45°-direction (violet and green triangles for liskene and tilene, respectively) and along the *y*-direction (black empty circles for the flakene architecture). The differently colored lines represent only a guideline for the eye. On the left and right sides of the image we report the simulation cells of liskene for different strain values and directions.

Furthermore, in figure 8 we report the stress–strain curves of flakene parent and daughter along the orthogonal directions *x* (empty squares) and *y* (empty circles) as their lattices display hexagonal symmetry. The mechanical characteristics of flakene parent are similar to those of graphene, showing a split between *x* (empty red squares) and *y* (empty green circles) curves at about 13% strain, and an almost linear regime up to 10% strain. However, the values of the strength are 60% lower than in the case of graphene (see table 3). Flakene daughter shows a behaviour comparable to graphene daughter, being characterized by a similar large presence of sp^2-carbon triangular lattices, with lower absolute values of the strength (see table 3).

Table 3: Loading direction (first column), Fracture strain (second column), strength (third column), strength$\times t$ (fourth column) and toughness$\times t$ (fifth column) of the parent and daughter planar structures alongside the specific strength and specific toughness (sixth and seventh columns). The ratio E/UTS is reported in the eighth column. The parameters *A* and *B* of the fit of the stress–strain curves (Eq. 3) are reported in the two last columns. The conventional thickness of the graphenic materials is considered to be $t = 3.35$ Å. In the table the following abbreviations were used: p.=parent, d.=daughter.

	Loading	Fracture	Strength	Strength	Toughness	Specific	Specific	E/UTS	A par.	B par.
	direction	strain		$\times t$	$\times t$	strength	toughness		of E_t fit	of E_t fit
		(%)	(GPa)	(N/m)	(J m^{-2})	(MN m kg^{-1})	(MJ kg^{-1})			
Graphene	x	$>$ 35	112	37.5	$>$ 9.83	49.7	$>$ 13.0	9.06	-2.57	1.39
	y	26-28	102	34.2	6.51	45.2	8.61	9.95	-2.22	-1.33
Graphene d.	x	18-20	29.3	9.81	0.83	19.2	1.62	9.11	2.15	-26.4
	y	$>$ 30	67.7	22.6	$>$ 3.63	44.3	$>$ 7.11	3.94	1.91	-8.26
Tilene p.	x,y	24-26	99.6	33.4	5.55	49.7	8.27	8.63	-1.37	-3.56
	45°	32-34	79.1	26.5	5.68	39.5	8.47	10.87	1.88	-11.0
Tilene	x,y	20-22	44.8	15.0	1.66	32.3	3.57	5.25	2.34	-12.9
	45°	18-20	30.3	10.2	0.92	21.9	1.97	7.76	11.3	-41.4
Flakene p.	x	22-24	66.7	22.3	3.37	37.2	5.61	9.18	-1.79	-2.37
	y	22-24	57.9	19.4	3.01	32.3	5.02	10.57	-0.90	-10.1
Flakene	x	12-14	23.6	7.92	0.49	18.7	1.16	4.87	19.4	-114
	y	14-16	25.8	8.63	0.63	20.4	1.49	4.46	15.5	-81.8
Lisken	x,y	18-20	63.2	21.2	2.19	35.8	3.70	6.52	1.7	-

e									2	14.0
	45°	14-16	43.8	14.7	1.27	24.7	2.14	9.40	2.49	-29.9
Liskene d.	x,y	12-14	27.8	9.32	0.59	18.5	1.20	11.15	-0.29	-8.68
	45°	14-16	28.0	9.37	0.68	19.0	1.37	11.07	5.45	-31.6

We notice that the augmentation procedure to obtain the liskene daughter architecture from liskene concerns only the carbon atoms that belong to the square shapes. In figure 9 we report the stress–strain curves of liskene and liskene daughter along the orthogonal *x*-(empty squares) and 45°-directions (empty circles). Even in this case we find the general trend previously observed of a decrease of the fracture strain and tensile strength from the parent to the daughter structure.
In figure 10 we present a comparison between the stress–strain characteristics along the *x* and *y* directions of liskene in comparison to tilene and flakene. As previously noticed, within the linear steep the uniaxial *x* (blue empty squares) and *y* (violet empty triangles) loading curves are overlapping, and at about 6% strain they fork and deviate progressively from linearity up to the fracture strain at about 14% and 18% strain, respectively. The values of liskene mechanical characteristics are slightly higher than the other proposed architectures (see table 3). We notice that after the disruption of the first set of bonds at 14% and 17% strain along the *x* and *y* directions respectively (see the structures reported in the left and right hand sides of 10), liskene stress–strain curves in both directions bounce into a second linear regime with different slope.
We notice that tilene parent (green line in Fig. 7) and liskene (red line in Fig. 9) basically present comparable stress–strain curves up to 10% strain. We rationalize this by noting that for both structures the stress–strain characteristics are initially dominated by the deformation of sp^2-carbon atom arranged in square forms. However, as the strain increases, the liskene stress–strain curve departs from that one of tilene parent. This is due to the fact that the former architecture undergoes the fracture of the bonds within the squares, and the stronger bounds of carbon triangles come into play.
The bifurcation shown in Figs. 6, 8, 9, and 10 is related to the symmetry of the unit cell of the materials. The symmetry imposes, within the linear regime, the equality of the elastic response along orthogonal directions for all the structures, while moving beyond the linear regime no constraints on the mechanical response exist.
As final remarks, we point out that the picture so far described, concerning the absolute values, slightly changes when we look at the specific properties reported in the seventh and eighth column of table 3. Indeed, the strength of our novel 2D structures is comparable to graphene, or even higher than the latter in the case of the tilene parent. Nevertheless, the trend of the specific toughness, which measures the ability of a material to absorb energy before fracture, is generally favourable to graphene with respect to the other structures.
Finally, we notice that Griffith [60] extrapolated from experimental data a maximum value of $UTS \approx E/9$. Later Polanyi and Orowan set $UTS \approx E/10$ from theoretical arguments. We notice that none of our structures go beyond the theoretical value of this cohesive strength and they are typically found in the range $E/11 \leq UTS \leq E/8$. However, there are some exceptions such as flakene for which $E/UTS \approx 4.87$ and 4.46 along *x*- and *y*-direction respectively, liskene with $E/UTS \approx 6.52$ along *x*-direction, and tilene with $E/UTS \approx 5.25$ along *x*-direction. We reported the values of E/UTS in the ninth column of Tab. 3 alongside the other mechanical characteristics. Our findings agree well with the trend given by Sun *et al.* [61], where structural arrangements characterised by sp carbon bonds, such as $Gr10$, show a significantly reduced Young's modulus but an undiminished UTS.

We found indeed that the square and triangular nodes are the most frequent points where our structures tend to break. The motivation of the failure is of course case dependent, nevertheless it can be generally attributed to two mechanisms. Indeed, the square and triangular nodes are characterised by high potential energy owing to the large angle strain (90° or 60° instead of 120°) and, thus, weaker bonds. Furthermore, also the alignment of bonds along the load direction influences the response. In this regard, the analysis of the non-linear parameters to identify changes in the material properties as the deformation progresses, particularly in large deformation regime, could be revealing. However, to establish universal relations between these parameters for quantifying nonlinear elastic responses in these novel bi-dimensional material is a cumbersome task, which goes beyond the scope of the present work more focused on methodological aspects. Nevertheless, we notice that the nonlinear behaviour of our materials is determined by reproducing the stress–strain curves. Thus, we present an analytical expression for the tangent modulus E_t. While for a wide set of materials a second order expression allows the fit of the stress–strain curves [62] up to the maximum stress, in order to properly describe the S-shape of the stress–strain of some materials under study we used a third order expression

$$\sigma(\epsilon) = E \cdot \epsilon \cdot \left(1 + A \cdot \epsilon + B \cdot \epsilon^2\right) \quad (3)$$

where E is the constant Young's modulus, ϵ is the uniaxial strain and A, B fitting parameters. In the case of the stress–strain curves along 45° direction the Young's modulus has been taken as a free parameter, otherwise it was taken from Tab. 2. The fit was performed only up to the strain corresponding to the maximum stress. From this fit, one can evaluate the tangent modulus $E_t = E \cdot \left(1 + 2A \cdot \epsilon + 3B \cdot \epsilon^2\right)$. The values of the parameters A and B are reported in the last two columns of Tab. 3. The R^2 of the fits are all higher than 0.99. The values of E for the stress–strain curves along the 45° direction are extracted from the fit. We found 407 GPa for tilene parent, 99.6 GPa for tilene, 413 GPa for liskene and 175 GPa for liskene daughter.

4. Routes to synthesis and application of graphene allotropes

Some concern is often raised on the experimental realization of theoretically proposed novel 2D carbon allotropes, whose potential is still hampered by the availability of synthesis effective routes. Standard approaches consist in exfoliation, or sono-chemical, chemical vapour deposition and lithographic methods [63], but typically work effectively only for graphene growth.
Nevertheless, recently several successful developments have been reported for the synthesis of complex structures by surface-assisted bottom-up routes [64, 65, 66, 67] that aim to assembly molecules on a metallic substrate, which catalyses the chemical reaction. In particular, these approaches are based on a specific combination of suitable precursors, diffusion and reaction barriers, catalytic properties of metallic substrates, and finally topology of the substrate surface to drive the formation of intricate carbon nanostructures [68]. These techniques made it possible the experimental realization of e.g. doped graphene nanoribbons [69], single-chirality nanotubes [70], and quantum dots [71, 72]. For example, the reproducible manufacturing of graphene nanoribbons with different topologies and widths has been achieved via a bottom-up approach based on the surface-assisted coupling [69, 70] of molecular precursors, such as the hexaiodo substituted macrocycle cyclohexa-m-phenylene (CHP) into covalently bonded polyphenylene networks and their subsequent cyclodehydrogenation on Cu(111), Au(111), and Ag(111) surfaces.
Another route to build up 2D carbon allotropes of different geometrical shapes could be pursued by sublimating precursor monomers functionalized with halogen species, such as Br, on a solid surface. The molecular building blocks, after removal of the halogen atom by thermal activation, form bi-radical surface-stabilized intermediate species able to diffuse across the substrate surface and to covalently link via radical addition reactions in aromatic chains, whose final geometry is dictated by the i) functionalized precursor shape, and ii) surface characteristics. By tuning the latter two variables, for example by using cycloalkanes, such as cyclopropane or cyclopropenium ions, and different metallic substrates one can in principle design a wide range of different 2D carbon allotropes.

Furthermore, very recent results were reported concerning the synthesis of other 2D carbon allotropes, such as the radiaannulene oligomers by iterative acetylenic coupling reactions [73]. These oligomers have rectangular rather than the hexagonal symmetry of graphene, and their geometry is obtained by adding sp-hybridized carbon atoms into the sp^2-carbon graphene framework. In particular the 6,6,12-graphyne carbon allotrope was synthesised by using iterative series of Pd-catalyzed Sonogashira coupling reactions between terminal alkynes and a suitable vinyl- or arylhalide (Br, I) electrophile.

Finally, we remind that the augmentation procedure to produce our daughter architectures induces a flat band in the band structure, similarly to the Kagome lattice. Dimerized Kagome lattices were experimentally realized [74] e.g. by placing CO molecules on Cu(111) into an anti-lattice configuration of the Kagome geometry to act as repulsive barriers to the 2D electron gas at the Cu(111) surface. The latter approach to the synthesis of Kagome lattices may represent thus a further route to the experimental realization of our structures.

Summarizing, we devise that a bottom-up approach can be used to achieve the atomically precise fabrication of our graphene 2D allotropes, enabling detailed experimental investigations of the properties of this exciting new class of materials.

The synthesis of novel stable 2D carbon allotropes characterised by low density, while retaining possibly the wonderful specific mechanical properties of graphene, could be beneficial for many fields, such as aeronautics, as it enables to fabricate light-weight materials having high stiffness, strength and toughness. In particular, the theoretical cohesive strength of a brittle defectless solid is approximately in the range of $E/10$ [60]. Our daughter structures typically fall in this range. In this regard, they could find application as wear-resistant structural materials. Nevertheless, depending on the loading axis they also display remarkable strength and toughness, whereby they could be also used as energy absorbers.

In addition, owing to a high surface-to-volume ratio, they can be useful for surface-based sensing mechanisms.

We also stress that owing to the augmentation procedure a FB emerges in the electronic band structure of daughter geometries, similarly to that found in frustrated Kagome lattices. The formation mechanism of this topologically nontrivial dispersionless band has been rationalized in terms of destructive interference of the electronic wavefunctions with only nearest-neighbor (NN) hopping. Consequently, fractional quantum Hall states are expected to emerge as the electronic FB mimics the Landau levels without the need of a magnetic field.

The non-trivial topological electronic structure emerging in the daughter lattice could have potential applications in low energy consumption electronics and spintronics devices, as much the recently discovered magnetic topological insulators [51, 75]. Furthermore, novel electronic states could be created via interlayer twisting by manipulating interlayer interactions. Also this exotic electronic behaviour could lead to dispersionless plasmons and polaritons.

From the fundamental physics point of view, these non-trivial topologies could represent a suitable platform for understanding the behaviour of complex quantum materials, nowadays mostly based on ultracold atoms in optical lattices and photonic devices. Simulating topological states is indeed one of the holy grails in condensed matter.

Finally, the fascinating mechanical and electronic characteristics of these graphene allotropes could be combined and have far-reaching impact on a variety of fields. For example, these intrinsic properties could lead to their implementation in devices integrating electrical and mechanical functionality on the nanoscale, such as in NEMS technologies. Additionally, due to the different mechanical response to loading along different directions, the interplay between mechanical and electronic properties could lead to a direction-dependent electronic conduction.

5. Conclusion

To conclude, in this work we present a method for designing thermodynamically stable all-sp^2 carbon allotropes with density lower than graphene and we fully characterize them from first-principles simulations.

In particular, we argue that flakene represents the least dense possible structure among the families of

all-sp^2 generated carbon allotropic forms starting from planar parent architectures under the local stability constraint and that the specific strength of tilene parent is higher than that of graphene. Nevertheless, novel geometries could also be obtained by initiating the augmentation from non-planar architectures, e.g. from pentagraphene. The relevant atomic arrangement, which is named liskene, displays a high cohesive energy at a density lower than 22% with respect to graphene.
By comparing the specific Young's modulus of these structures with graphene, we notice that there is a threshold below which is not possible to reduce further the density without a considerable depletion of this elastic property. In particular, we found a reduction of about 40% of the specific Young's modulus below the liskene density. This can be clearly seen in the case of flakene, which displays the lowest density among the proposed planar structures as well as the smallest absolute and specific Young's modulus. Thus, we conclude that the search for materials with high specific Young's modulus should occur among the high-density carbon allotropes or proceed by changing the paradigm of interaction, for example by enhancing electrostatic and/or van der Waals interactions.
We also find that while the absolute mechanical characteristics of the proposed structures, such as fracture strain, strength, and toughness, deplete moving from parent to daughter architectures, their specific counterparts are comparable to those of graphene. In this regard, we conclude that our structures could be used to replace graphene when weight decrease is an issue of paramount importance.
We further notice the novel graphene allotropes are characterised by a higher Poisson ratio and low area density of atoms, leaving more free space for bond rotation. Thus, these geometries may lead to new strategies for enhancing the fracture strains of graphene allotropes. In this regard, the lower density of these graphene allotropes leaves more freedom with respect to graphene for further engineering or for further modifications by chemical functionalization. This would open up interesting prospects also in the adsorption and sieving of gases. We also stress that our augmentation method could be extended to design novel lightweight one-dimensional (carbon nanotubes) and three-dimensional (foams [76, 77]) carbon allotropes.
Furthermore, we find that owing to the presence of frustrated triangular shapes in the augmented structures a narrow band close to the Fermi level appears. We rationalized this behaviour as due to destructive interference of the electronic wavefunctions. In this respect, these architectures resemble Kagome lattices and this feature extends their use as topological materials or for revealing unexpected quantum phases of matter.
Finally, we believe that our proposed architectures could be synthesised via surface-assisted bottom-up techniques recently used to produce covalently-linked 2D polymers and carbon allotropes.

Acknowledgements

N.M.P. is supported by the European Commission under the Graphene Flagship Core 2 grant No. 785219 (WP14, "Composites"), the FET Proactive ("Neurofibres") grant No. 732344 as well as by the Italian Ministry of Education, University and Research (MIUR) under the "Departments of Excellence" grant L.232/2016, the ARS01-01384-PROSCAN and the PRIN-20177TTP3S grants. The authors gratefully acknowledge the Gauss Centre for Supercomputing for funding this project by providing computing time on the GCS Supercomputer JUQUEEN at Jülich Supercomputing Centre (JSC) [78]. Furthermore, the authors acknowledge Bruno Kessler Foundation (FBK) for providing unlimited access to the KORE computing facility.

References

[1] R. Hoffmann, A. A. Kabanov, A. A. Golov, D. M. Proserpio, Homo citans and carbon allotropes:

For an ethics of citation, Angewandte Chemie International Edition 55 (37) (2016) 10962–10976.

arXiv:https://onlinelibrary.wiley.com/doi/pdf/10.1002/anie.201600655

, doi:10.1002/anie.201600655.

URL https://onlinelibrary.wiley.com/doi/abs/10.1002/anie.201600655

[2] A. K. Geim, K. S. Novoselov, The rise of graphene, Nature Materials 6 (3) (2007) 183–191. doi:10.1038/nmat1849.
URL https://doi.org/10.1038/nmat1849

[3] S. Taioli, Computational study of graphene growth on copper by first-principles and kinetic Monte Carlo calculations, Journal of molecular modeling 20 (7) (2014) 2260.

[4] R. Tatti, L. Aversa, R. Verucchi, E. Cavaliere, G. Garberoglio, N. M. Pugno, G. Speranza, S. Taioli, Synthesis of single layer graphene on Cu (111) by C_{60} supersonic molecular beam epitaxy, RSC Advances 6 (44) (2016) 37982–37993.

[5] S. Taioli, A. Paris, L. Calliari, Characterization of pristine and functionalized graphene on metal surfaces by electron spectroscopy, in: Graphene Science Handbook: Size-Dependent Properties, Vol. 5, CRC Press 2016, Taylor & Francis Group, 2016, pp. 269–285.

[6] P. Umari, O. Petrenko, S. Taioli, M. M. De Souza, Communication: Electronic band gaps of semiconducting zig-zag carbon nanotubes from many-body perturbation theory calculations, The Journal of Chemical Physics 136 (18) (2012) 181101. arXiv:https://doi.org/10.1063/1.4716178, doi:10.1063/1.4716178.
URL https://doi.org/10.1063/1.4716178

[7] S. Taioli, P. Umari, M. De Souza, Electronic properties of extended graphene nanomaterials from GW calculations, physica status solidi (b) 246 (11-12) (2009) 2572–2576.

[8] D. Haberer, L. Petaccia, M. Farjam, S. Taioli, S. Jafari, A. Nefedov, W. Zhang, L. Calliari, G. Scarduelli, B. Dora, et al., Direct observation of a dispersionless impurity band in hydrogenated graphene, Physical Review B 83 (16) (2011) 165433.

[9] M. J. Allen, V. C. Tung, R. B. Kaner, Honeycomb carbon: A review of graphene, Chemical Reviews 110 (1) (2010) 132–145. doi:10.1021/cr900070d.
URL https://doi.org/10.1021/cr900070d

[10] E. P. Randviir, D. A. Brownson, C. E. Banks, A decade of graphene research: production, applications and outlook, Materials Today 17 (9) (2014) 426 – 432. doi:https://doi.org/10.1016/j.mattod.2014.06.001.
URL http://www.sciencedirect.com/science/article/pii/S1369702114002144

[11] S. Signetti, S. Taioli, N. M. Pugno, 2d material armors showing superior impact strength of few layers, ACS Applied Materials & Interfaces 9 (46) (2017) 40820–40830. arXiv:https://doi.org/10.1021/acsami.7b12030,

doi:10.1021/acsami.7b12030.
URL https://doi.org/10.1021/acsami.7b12030

[12] E. Lepore, F. Bosia, F. Bonaccorso, M. Bruna, S. Taioli, G. Garberoglio, A. C. Ferrari, N. M. Pugno, Spider silk reinforced by graphene or carbon nanotubes, 2D Materials 4 (3) (2017) 031013.
URL http://stacks.iop.org/2053-1583/4/i=3/a=031013

[13] M. Azzolini, T. Morresi, K. Abrams, R. Masters, N. Stehling, C. Rodenburg, N. M. Pugno, S. Taioli, M. Dapor, Anisotropic approach for simulating electron transport in layered materials: Computational and experimental study of highly oriented pyrolitic graphite, The Journal of Physical Chemistry C 122 (18) (2018) 10159–10166.
arXiv:https://doi.org/10.1021/acs.jpcc.8b02256,
doi:10.1021/acs.jpcc.8b02256.
URL https://doi.org/10.1021/acs.jpcc.8b02256

[14] M. Azzolini, T. Morresi, G. Garberoglio, L. Calliari, N. M. Pugno, S. Taioli, M. Dapor, Monte Carlo simulations of measured electron energy-loss spectra of diamond and graphite: Role of dielectric-response models, Carbon 118 (aaa) (2017) 299 – 309.
doi:https://doi.org/10.1016/j.carbon.2017.03.041.
URL
http://www.sciencedirect.com/science/article/pii/S0008622317302816

[15] D. Haberer, D. Vyalikh, S. Taioli, B. Dora, M. Farjam, J. Fink, D. Marchenko, T. Pichler, K. Ziegler, S. Simonucci, et al., Tunable band gap in hydrogenated quasi-free-standing graphene, Nano letters 10 (9) (2010) 3360–3366.

[16] C. Tan, H. Zhang, Two-dimensional transition metal dichalcogenide nanosheet-based composites, Chem. Soc. Rev. 44 (aaa) (2015) 2713–2731. doi:10.1039/C4CS00182F.
URL http://dx.doi.org/10.1039/C4CS00182F

[17] P. Vogt, P. De Padova, C. Quaresima, J. Avila, E. Frantzeskakis, M. C. Asensio, A. Resta, B. Ealet, G. Le Lay, Silicene: Compelling experimental evidence for Graphenelike two-dimensional silicon, Phys. Rev. Lett. 108 (aaa) (2012) 155501. doi:10.1103/PhysRevLett.108.155501.
URL https://link.aps.org/doi/10.1103/PhysRevLett.108.155501

[18] X. Chen, Q. Yang, R. Meng, J. Jiang, Q. Liang, C. Tan, X. Sun, The electronic and optical properties of novel germanene and antimonene heterostructures, J. Mater. Chem. C 4 (aaa) (2016) 5434–5441. doi:10.1039/C6TC01141A.
URL http://dx.doi.org/10.1039/C6TC01141A

[19] L. Matthes, O. Pulci, F. Bechstedt, Massive Dirac quasiparticles in the optical absorbance of graphene, silicene, germanene, and tinene, Journal of Physics: Condensed Matter 25 (39) (2013) 395305.
URL http://stacks.iop.org/0953-8984/25/i=39/a=395305

[20] N. e. a. Mounet, Two-dimensional materials from high-throughput computational exfoliation of experimentally known compounds, Nature Nanotechnology 13 (aaa) (2018) 246–252. doi:10.1038/s41565-017-0035-5.
URL https://doi.org/10.1038/s41565-017-0035-5

[21] N. Nosengo, Can artificial intelligence create the next wonder material?, Nature 533 (aaa) (2010) 23 – 26.

[22] A. K. Geim, I. V. Grigorieva, Van der Waals heterostructures, Nature 499 (aaa) (2013) 419. doi:10.1038/nature12385.
URL http://dx.doi.org/10.1038/nature12385

[23] J. C. Meyer, A. Chuvilin, G. Algara-Siller, J. Biskupek, U. Kaiser, Selective sputtering and atomic resolution imaging of atomically thin boron nitride membranes, Nano Letters 9 (7) (2009) 2683–2689, pMID: 19480400. arXiv:https://doi.org/10.1021/nl9011497, doi:10.1021/nl9011497.
URL https://doi.org/10.1021/nl9011497

[24] Y. Liu, G. Wang, Q. Huang, L. Guo, X. Chen, Structural and electronic properties of T graphene: A two-dimensional carbon allotrope with tetrarings, Phys. Rev. Lett. 108 (aaa) (2012) 225505. doi:10.1103/PhysRevLett.108.225505.
URL https://link.aps.org/doi/10.1103/PhysRevLett.108.225505

[25] L.-C. Xu, R.-Z. Wang, M.-S. Miao, X.-L. Wei, Y.-P. Chen, H. Yan, W.-M. Lau, L.-M. Liu, Y.-M. Ma, Two dimensional Dirac carbon allotropes from graphene, Nanoscale 6 (aaa) (2014) 1113–1118. doi:10.1039/C3NR04463G.
URL http://dx.doi.org/10.1039/C3NR04463G

[26] H. Huang, W. Duan, Z. Liu, The existence/absence of Dirac cones in graphynes, New Journal of Physics 15 (2) (2013) 023004.
URL http://stacks.iop.org/1367-2630/15/i=2/a=023004

[27] S. Taioli, R. Gabbrielli, S. Simonucci, N. M. Pugno, A. Iorio, Lobachevsky crystallography made real through carbon pseudospheres, Journal of Physics: Condensed Matter 28 (13) (2016) 13LT01.
URL http://stacks.iop.org/0953-8984/28/i=13/a=13LT01

[28] S. Torquato, F. H. Stillinger, Jammed hard-particle packings: From Kepler to Bernal and beyond, Rev. Mod. Phys. 82 (aaa) (2010) 2633–2672. doi:10.1103/RevModPhys.82.2633.
URL https://link.aps.org/doi/10.1103/RevModPhys.82.2633

[29] A. Thue, Über die dichteste zusammenstellung von kongruenten kreisen in einer ebene, Norske Vid. Selsk. Skr (No. 1) (1910) pp. 1–9.

[30] J. L. Lagrange, Recherches d'arithmétique, Nouv. Mém. Acad. Roy. Soc. Belles Lettres (1773) pp. 265–312.

[31] L. F. Tóth, Über die dichteste kugellagerung, Math 48 (1943) 676.

[32] K. Böröczky, Über stabile kreis und kugelsysteme, Ann. Univ. Sci. Budapest Eötvös Sect. Math (7) (1964) 79.

[33] P. G. et al., Quantum espresso: a modular and open-source software project for quantum simulations of materials, Journal of Physics: Condensed Matter 21 (39) (2009) 395502.
URL http://stacks.iop.org/0953-8984/21/i=39/a=395502

[34] H. Sun, S. Mukherjee, M. Daly, A. Krishnan, M. H. Karigerasi, C. V. Singh, New insights into the structure-nonlinear mechanical property relations for graphene allotropes, Carbon 110 (aaa) (2016) 443 – 457. doi:https://doi.org/10.1016/j.carbon.2016.09.018.
URL
http://www.sciencedirect.com/science/article/pii/S0008622316307692

[35] G. Brunetto, P. A. S. Autreto, L. D. Machado, B. I. Santos, R. P. B. dos Santos, D. S. Galvão, Nonzero gap two-dimensional carbon allotrope from porous graphene, The Journal of Physical Chemistry C 116 (23) (2012) 12810–12813.
arXiv:https://doi.org/10.1021/jp211300n, doi:10.1021/jp211300n.
URL https://doi.org/10.1021/jp211300n

[36] E. Perim, R. Paupitz, P. A. S. Autreto, D. S. Galvao, Inorganic graphenylene: A porous two-dimensional material with tunable band gap, The Journal of Physical Chemistry C 118 (41) (2014) 23670–23674. arXiv:https://doi.org/10.1021/jp502119y,
doi:10.1021/jp502119y.
URL https://doi.org/10.1021/jp502119y

[37] Y. J. Dappe, R. Oszwaldowski, P. Pou, J. Ortega, R. Pérez, F. Flores, Local-orbital occupancy formulation of density functional theory: Application to Si, C, and graphene, Phys. Rev. B 73 (aaa) (2006) 235124. doi:10.1103/PhysRevB.73.235124.
URL https://link.aps.org/doi/10.1103/PhysRevB.73.235124

[38] I. A. Pašti, A. Jovanović, A. S. Dobrota, S. V. Mentus, B. Johansson, N. V. Skorodumova, Atomic adsorption on pristine graphene along the periodic table of elements – from PBE to non-local functionals, Applied Surface Science 436 (aaa) (2018) 433 – 440. doi:https://doi.org/10.1016/j.apsusc.2017.12.046.
URL http://www.sciencedirect.com/science/article/pii/S0169433217336334

[39] Q. Song, B. Wang, K. Deng, X. Feng, M. Wagner, J. D. Gale, K. Müllen, L. Zhi, Graphenylene, a unique two-dimensional carbon network with nondelocalized cyclohexatriene units, J. Mater. Chem. C 1 (aaa) (2013) 38–41. doi:10.1039/C2TC00006G.
URL http://dx.doi.org/10.1039/C2TC00006G

[40] S. Zhang, J. Zhou, Q. Wang, X. Chen, Y. Kawazoe, P. Jena, Penta-graphene: A new carbon allotrope, Proceedings of the National Academy of Sciences 112 (8) (2015) 2372–2377. arXiv:http://www.pnas.org/content/112/8/2372.full.pdf, doi:10.1073/pnas.1416591112.
URL http://www.pnas.org/content/112/8/2372

[41] J. Maultzsch, S. Reich, C. Thomsen, H. Requardt, P. Ordejón, Phonon dispersion in graphite, Phys. Rev. Lett. 92 (2004) 075501. doi:10.1103/PhysRevLett.92.075501.
URL https://link.aps.org/doi/10.1103/PhysRevLett.92.075501

[42] P. Pavone, R. Bauer, K. Karch, O. Schütt, S. Vent, W. Windl, D. Strauch, S. Baroni, S. de Gironcoli, Ab initio phonon calculations in solids, Physica B: Condensed Matter 219-220 (1996) 439 – 441, pHONONS 95. doi:https://doi.org/10.1016/0921-4526(95)00771-7.
URL http://www.sciencedirect.com/science/article/pii/0921452695007717

[43] O. Dubay, G. Kresse, Accurate density functional calculations for the phonon dispersion relations of graphite layer and carbon nanotubes, Phys. Rev. B 67 (2003) 035401. doi:10.1103/PhysRevB.67.035401.
URL https://link.aps.org/doi/10.1103/PhysRevB.67.035401

[44] C. P. J. Marquina, J. González, Espectroscopia raman del grafeno monocapa y el grafito: Acoplamiento electrón fonon y efectos no adiabáticos, Revista Tumbaga 1 (5) (2010) 183–194.

[45] D. Sánchez-Portal, E. Artacho, J. M. Soler, A. Rubio, P. Ordejón, Ab initio structural, elastic, and vibrational properties of carbon nanotubes, Phys. Rev. B 59 (1999) 12678–12688. doi:10.1103/PhysRevB.59.12678.
URL https://link.aps.org/doi/10.1103/PhysRevB.59.12678

[46] Y. Miyamoto, M. L. Cohen, S. G. Louie, Ab initio calculation of phonon spectra for graphite, bn, and bc_2n sheets, Phys. Rev. B 52 (1995) 14971–14975. doi:10.1103/PhysRevB.52.14971.
URL https://link.aps.org/doi/10.1103/PhysRevB.52.14971

[47] Y. Xu, C. Q. Chen, X. Tian, Wave characteristics of two-dimensional hierarchical hexagonal lattice structures, Journal of Vibration and Acoustics 136 (aaa) (2013) 011011. doi:10.1115/1.4025550.
URL http://dx.doi.org/10.1115/1.4025550

[48] P. G. Martinsson, A. B. Movchan, Vibrations of lattice structures and phononic band gaps, The Quarterly Journal of Mechanics and Applied Mathematics 56 (1) (2003) 45–64. arXiv:http://oup.prod.sis.lan/qjmam/article-pdf/56/1/45/5198955/560045.pdf, doi:10.1093/qjmam/56.1.45.
URL https://doi.org/10.1093/qjmam/56.1.45

[49] A. H. Castro Neto, F. Guinea, N. M. R. Peres, K. S. Novoselov, A. K. Geim, The electronic properties of graphene, Rev. Mod. Phys. 81 (aaa) (2009) 109–162. doi:10.1103/RevModPhys.81.109.
URL https://link.aps.org/doi/10.1103/RevModPhys.81.109

[50] Z. e. a. Lin, Flatbands and emergent ferromagnetic ordering in fe_3sn_2 Kagome lattices, Phys. Rev. Lett. 121 (aaa) (2018) 096401. doi:10.1103/PhysRevLett.121.096401.
URL https://link.aps.org/doi/10.1103/PhysRevLett.121.096401

[51] Z. Li, J. Zhuang, L. Wang, H. Feng, Q. Gao, X. Xu, W. Hao, X. Wang, C. Zhang, K. Wu, S. X. Dou, L. Chen, Z. Hu, Y. Du, Realization of flat band with possible nontrivial topology in electronic kagome lattice, Science Advances 4 (11). arXiv:https://advances.sciencemag.org/content/4/11/eaau4511.full.pdf, doi:10.1126/sciadv.aau4511.
URL https://advances.sciencemag.org/content/4/11/eaau4511

[52] D. L. Bergman, C. Wu, L. Balents, Band touching from real-space topology in frustrated hopping models, Phys. Rev. B 78 (aaa) (2008) 125104. doi:10.1103/PhysRevB.78.125104.
URL https://link.aps.org/doi/10.1103/PhysRevB.78.125104

[53] H. Huntington, The elastic constants of crystals, Vol. 7 of Solid State Physics, Academic Press, 1958, pp. 213 – 351. doi:https://doi.org/10.1016/S0081-1947(08)60553-6.
URL http://www.sciencedirect.com/science/article/pii/S0081194708605536

[54] X.-L. Sheng, H.-J. Cui, F. Ye, Q.-B. Yan, Q.-R. Zheng, G. Su, Octagraphene as a versatile carbon atomic sheet for novel nanotubes, unconventional fullerenes, and hydrogen storage, Journal of Applied Physics 112 (7) (2012) 074315. arXiv:https://doi.org/10.1063/1.4757410, doi:10.1063/1.4757410.
URL https://doi.org/10.1063/1.4757410

[55] F. Thorpe, I. Jasiuk, New results in the theory of elasticity for two-dimensional composites, Proceedings of the Royal Society of London A: Mathematical, Physical and Engineering Sciences 438 (1904) (1992) 531–544.
arXiv:http://rspa.royalsocietypublishing.org/content/438/1904/531.full.pdf, doi:10.1098/rspa.1992.0124.
URL http://rspa.royalsocietypublishing.org/content/438/1904/531

[56] C. Lee, X. Wei, J. W. Kysar, J. Hone, Measurement of the elastic properties and intrinsic strength of monolayer graphene, Science 321 (5887) (2008) 385–388.
arXiv:https://science.sciencemag.org/content/321/5887/385.full.pdf, doi:10.1126/science.1157996.
URL https://science.sciencemag.org/content/321/5887/385

[57] E. Cadelano, P. L. Palla, S. Giordano, L. Colombo, Nonlinear elasticity of monolayer graphene, Phys. Rev. Lett. 102 (2009) 235502. doi:10.1103/PhysRevLett.102.235502.
URL https://link.aps.org/doi/10.1103/PhysRevLett.102.235502

[58] M. Xu, J. T. Paci, J. Oswald, T. Belytschko, A constitutive equation for graphene based on density functional theory, International Journal of Solids and Structures 49 (18) (2012) 2582 – 2589.
doi:https://doi.org/10.1016/j.ijsolstr.2012.05.019.
URL
http://www.sciencedirect.com/science/article/pii/S0020768312002296

[59] B. Hajgató, S. Güryel, Y. Dauphin, J.-M. Blairon, H. E. Miltner, G. Van Lier, F. De Proft, P. Geerlings, Theoretical investigation of the intrinsic mechanical properties of single- and double-layer graphene, The Journal of Physical Chemistry C 116 (42) (2012) 22608–22618.
arXiv:https://doi.org/10.1021/jp307469u, doi:10.1021/jp307469u.
URL https://doi.org/10.1021/jp307469u

[60] G. A. Arnold, T. G. Ingram, The phenomena of rupture and flow in solids, Philosophical Transactions of the Royal Society of London. Series A 221.

[61] H. Sun, S. Mukherjee, Z. Shi, C. V. Singh, Elastomer-like deformation in high-poisson's-ratio graphene allotropes may allow tensile strengths beyond theoretical cohesive strength limits, Carbon 143 (2019) 752 – 761. doi:https://doi.org/10.1016/j.carbon.2018.11.079.

URL
http://www.sciencedirect.com/science/article/pii/S0008622318311126

[62] N. Pugno, F. Marino, A. Carpinteri, Towards a periodic table for the nanomechanical properties of the elements, International Journal of Solids and Structures 43 (18) (2006) 5647 – 5657. doi:https://doi.org/10.1016/j.ijsolstr.2005.12.003.
URL
http://www.sciencedirect.com/science/article/pii/S0020768305006360

[63] C. Backes, A. Abdelkader, C. Alonso, A. Andrieux, R. Arenal, J. Azpeitia, N. Balakrishnan, L. Banszerus, J. Barjon, R. Bartali, et al., Production and processing of graphene and related materials.

[64] M. Bieri, M. Treier, J. Cai, K. Aït-Mansour, P. Ruffieux, O. Gröning, P. Gröning, M. Kastler, R. Rieger, X. Feng, K. Müllen, R. Fasel, Porous graphenes: two-dimensional polymer synthesis with atomic precision, Chem. Commun. (2009) 6919–6921doi:10.1039/B915190G.
URL http://dx.doi.org/10.1039/B915190G

[65] M. Bieri, M.-T. Nguyen, O. Gröning, J. Cai, M. Treier, K. Aït-Mansour, P. Ruffieux, C. A. Pignedoli, D. Passerone, M. Kastler, K. Müllen, R. Fasel, Two-dimensional polymer formation on surfaces: Insight into the roles of precursor mobility and reactivity, Journal of the American Chemical Society 132 (46) (2010) 16669–16676, pMID: 21043454.
arXiv:https://doi.org/10.1021/ja107947z, doi:10.1021/ja107947z.
URL https://doi.org/10.1021/ja107947z

[66] J. Cai, P. Ruffieux, R. Jaafar, M. Bieri, T. Braun, S. Blankenburg, M. Muoth, A. P. Seitsonen, M. Saleh, X. Feng, K. Müllen, R. Fasel, Atomically precise bottom-up fabrication of graphene nanoribbons, Nature 466. doi:10.1038/nature09211.
URL https://doi.org/10.1038/nature09211

[67] M. L. Álvares Paz, A. Saraiva-Souza, V. Meunier, E. C. G. ao, Naphthylenes: 1d and 2d carbon allotropes based on naphthyl units, Carbon 153 (2019) 792 – 803. doi:https://doi.org/10.1016/j.carbon.2019.07.037.
URL
http://www.sciencedirect.com/science/article/pii/S0008622319307249

[68] P. S. C.-A. Palma, Blueprinting macromolecular electronics, Nature Chemistry 3 (2011) 431.

[69] Graphene nanoribbon heterojunctions, Nature Nanotechnology 9 (2014) 896.

[70] Controlled synthesis of single-chirality carbon nanotubes, Nature 512.

[71] E. Carbonell-Sanromà, P. Brandimarte, R. Balog, M. Corso, S. Kawai, A. Garcia-Lekue, S. Saito, S. Yamaguchi, E. Meyer, D. Sánchez-Portal, J. I. Pascual, Quantum dots embedded in graphene nanoribbons by chemical substitution, Nano Letters 17 (1) (2017) 50–56, pMID: 28073274. arXiv:https://doi.org/10.1021/acs.nanolett.6b03148, doi:10.1021/acs.nanolett.6b03148.
URL https://doi.org/10.1021/acs.nanolett.6b03148

[72] S. Wang, N. Kharche, E. Costa Girão, X. Feng, K. Müllen, V. Meunier, R. Fasel, P. Ruffieux, Quantum dots in graphene nanoribbons, Nano Letters 17 (7) (2017) 4277–4283, pMID: 28603996. arXiv:https://doi.org/10.1021/acs.nanolett.7b01244, doi:10.1021/acs.nanolett.7b01244.
URL https://doi.org/10.1021/acs.nanolett.7b01244

[73]Synthesis of radiaannulene oligomers to model the elusive carbon allotrope 6,6,12-graphyne, Nature Communications 10. doi:10.1038/s41467-019-11700-0.
URL https://doi.org/10.1038/s41467-019-11700-0

[74] Robust zero-energy modes in an electronic higher-order topological insulator, Nature Materials 18 (2019) 1292.

[75] K. S. K. C. e. a. Baidya, S., Chern insulator with a nearly flat band in the metal-organic-framework-based kagome lattice, Sci. Rep. 9 (2019) 13807.

[76] A. Pedrielli, S. Taioli, G. Garberoglio, N. M. Pugno, Mechanical and thermal properties of graphene random nanofoams via molecular dynamics simulations, Carbon 132 (aaa) (2018) 766–775. doi:https://doi.org/10.1016/j.carbon.2018.02.081.
URL
http://www.sciencedirect.com/science/article/pii/S0008622318302112

[77] A. Pedrielli, S. Taioli, G. Garberoglio, N. M. Pugno, Designing graphene based nanofoams with nonlinear auxetic and anisotropic mechanical properties under tension or compression, Carbon 111 (aaa) (2017) 796 – 806. doi:https://doi.org/10.1016/j.carbon.2016.10.034.
URL
http://www.sciencedirect.com/science/article/pii/S0008622316308946

[78] J. S. Centre, JUQUEEN: IBM Blue Gene/Q Supercomputer System at the Jülich Supercomputing Centre, Journal of large-scale research facilities 1 (A1). doi:10.17815/jlsrf-1-18.
URL http://dx.doi.org/10.17815/jlsrf-1-18

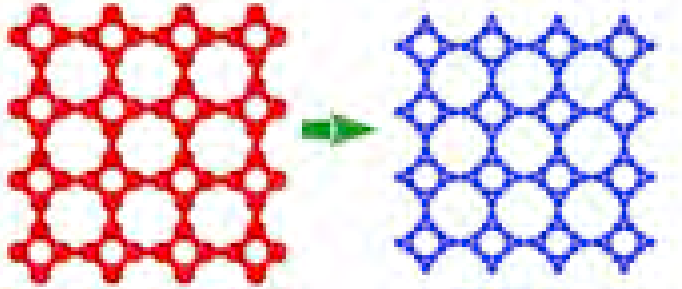

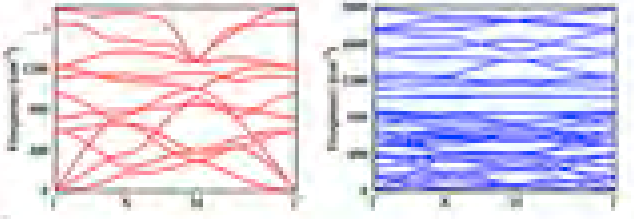

Stability

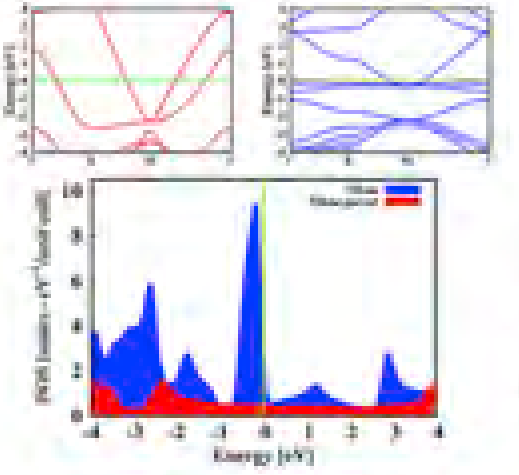

Frustration

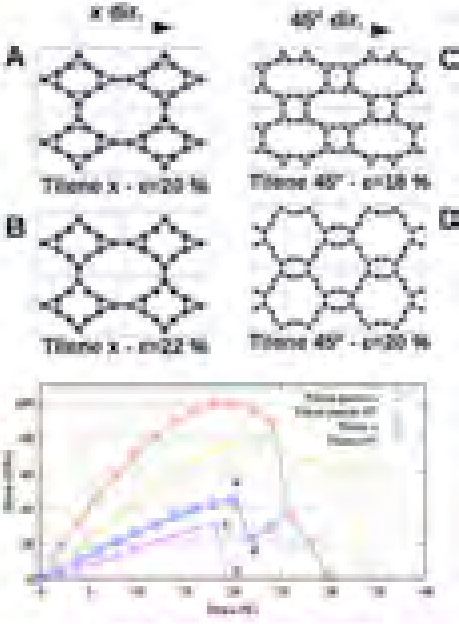

Strength

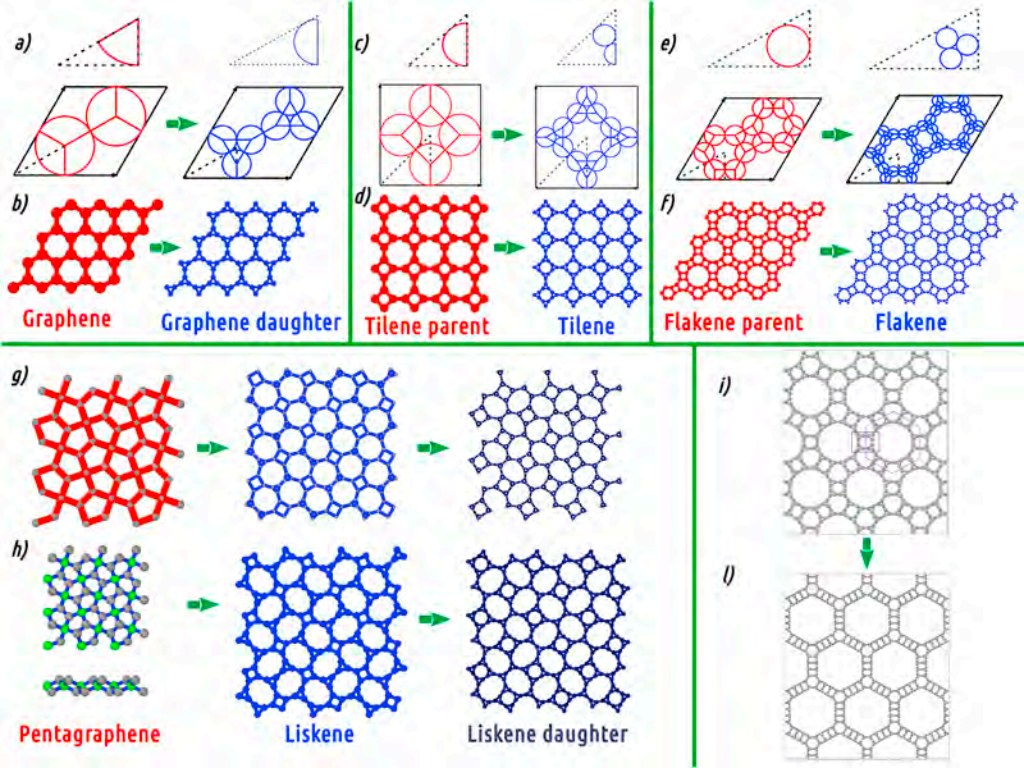
a)
b)
Graphene
Graphene daughter
c)
d)
Tilene parent
Tilene
e)
f)
Flakene parent
Flakene
g)
h)
Pentagraphene
Liskene
Liskene daughter
i)
l)

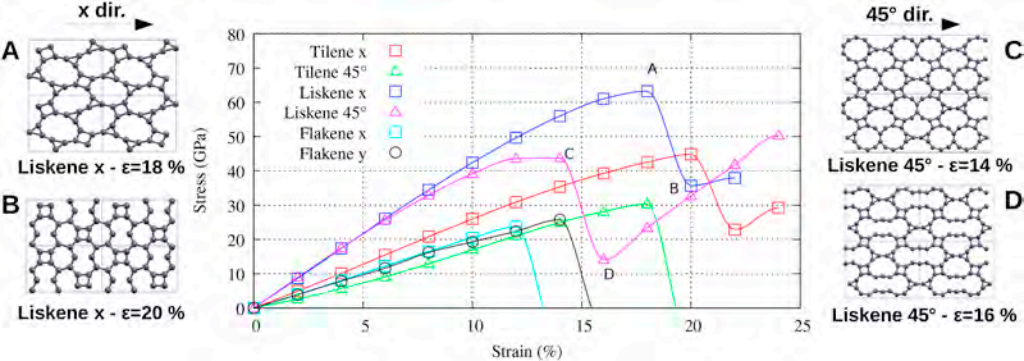
x dir.
A
Liskene x - ε=18 %
B
Liskene x - ε=20 %
Tilene x
Tilene 45°
Liskene x
Liskene 45°
Flakene x
Flakene y
Stress (GPa)
Strain (%)
A
B
C
D
45° dir.
C
Liskene 45° - ε=14 %
D
Liskene 45° - ε=16 %

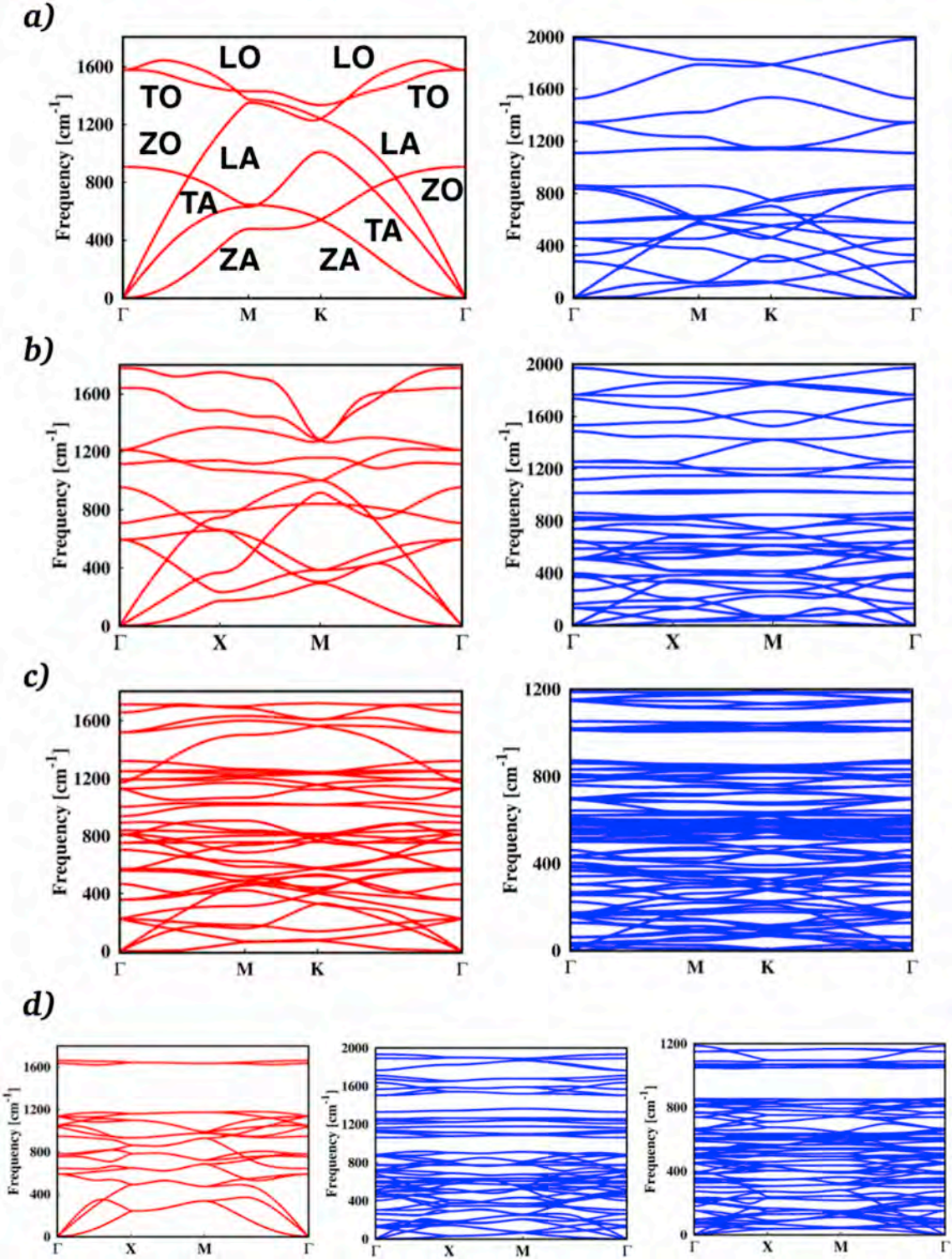
a)
LO
LO
TO
TO
ZO
LA
LA
TA
ZO
TA
ZA
ZA
Frequency [cm^{-1}]
Γ
M
K
b)
X
c)
d)

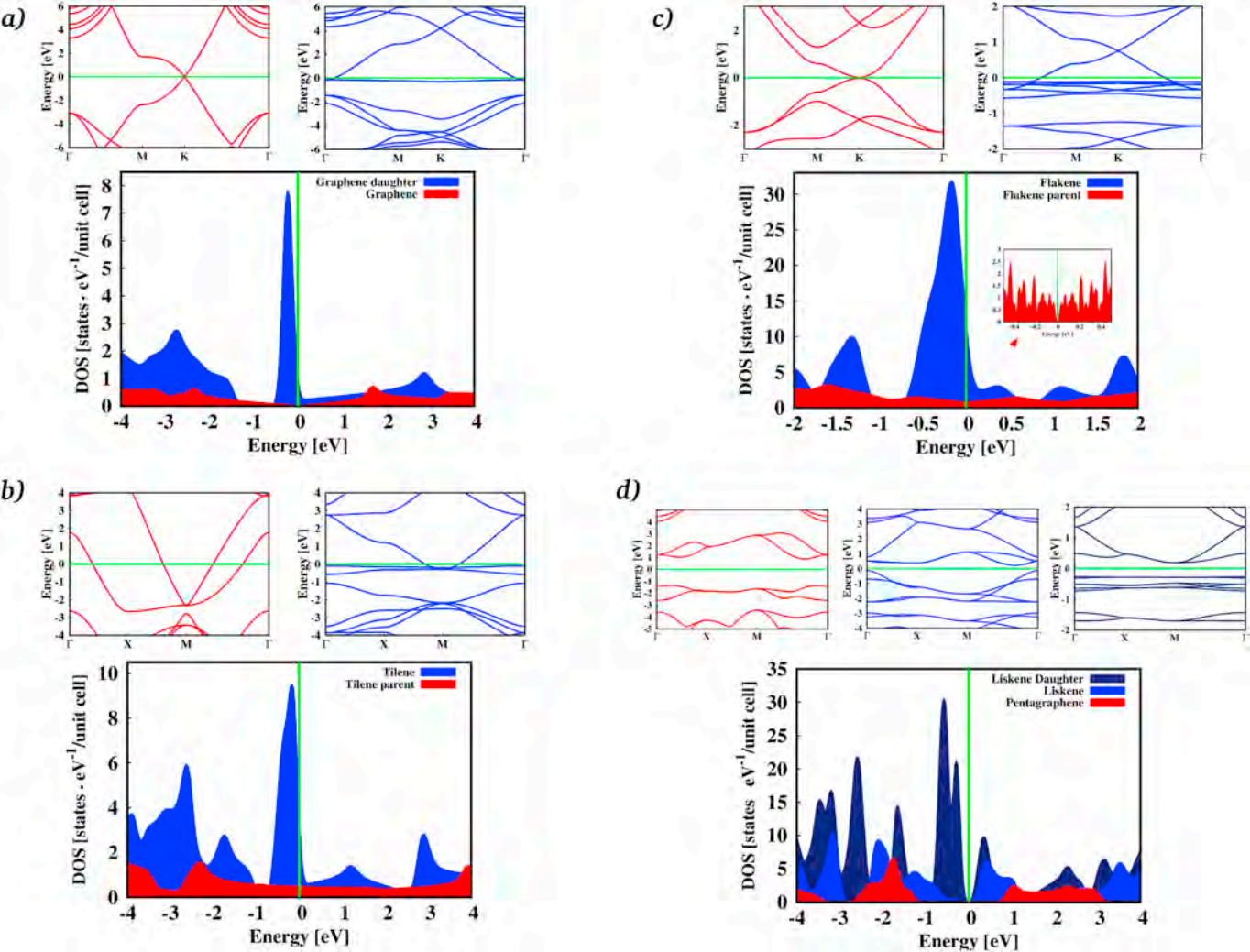
a)
Energy [eV]
Γ M K Γ
Graphene daughter
Graphene
DOS [states · eV⁻¹/unit cell]
Energy [eV]
b)
Γ X M Γ
Tilene
Tilene parent
c)
Flakene
Flakene parent
d)
Liskene Daughter
Liskene
Pentagraphene

a)

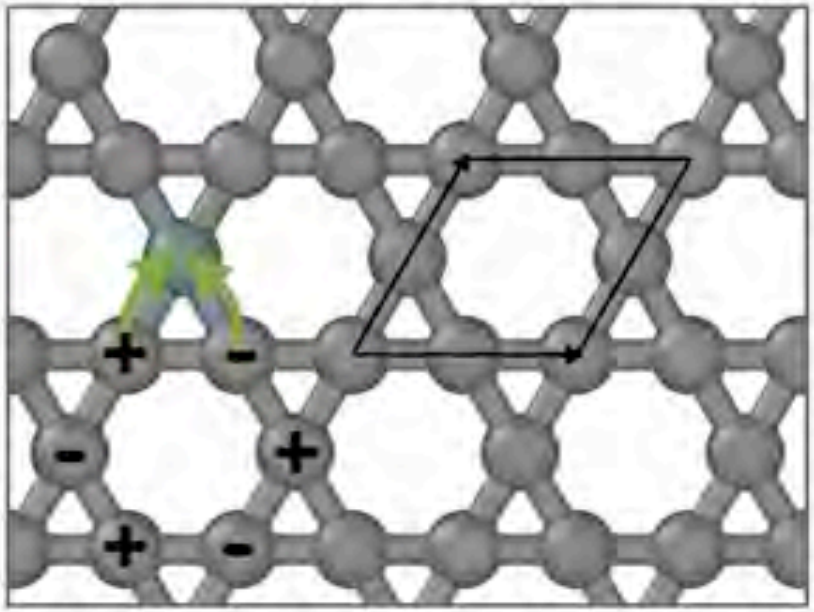
Kagome lattice
+
-
-
+
+
-

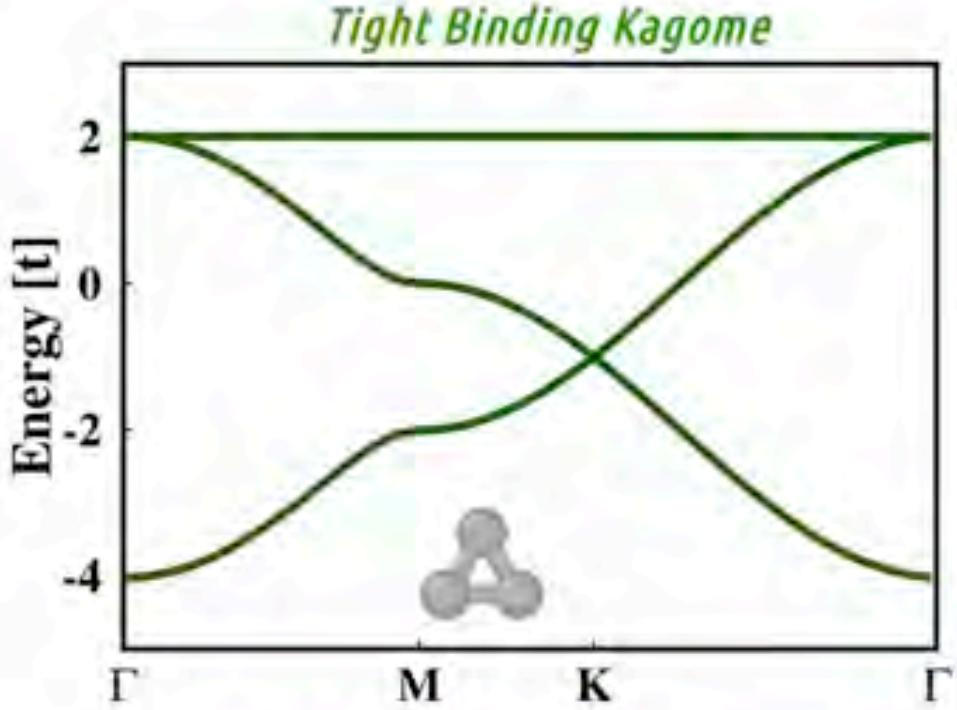
Tight Binding Kagome
Energy [t]
2
0
-2
-4
Γ
M
K
Γ

b)

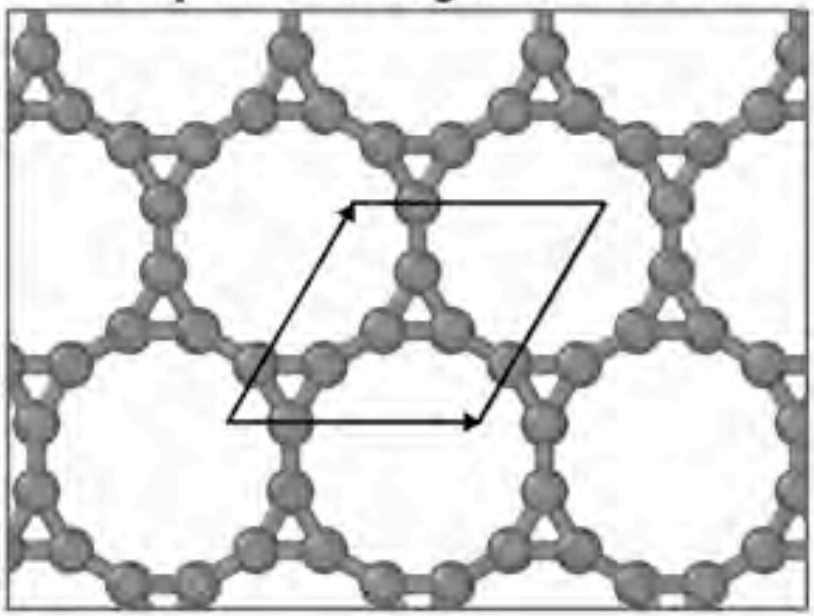
Graphene daughter lattice

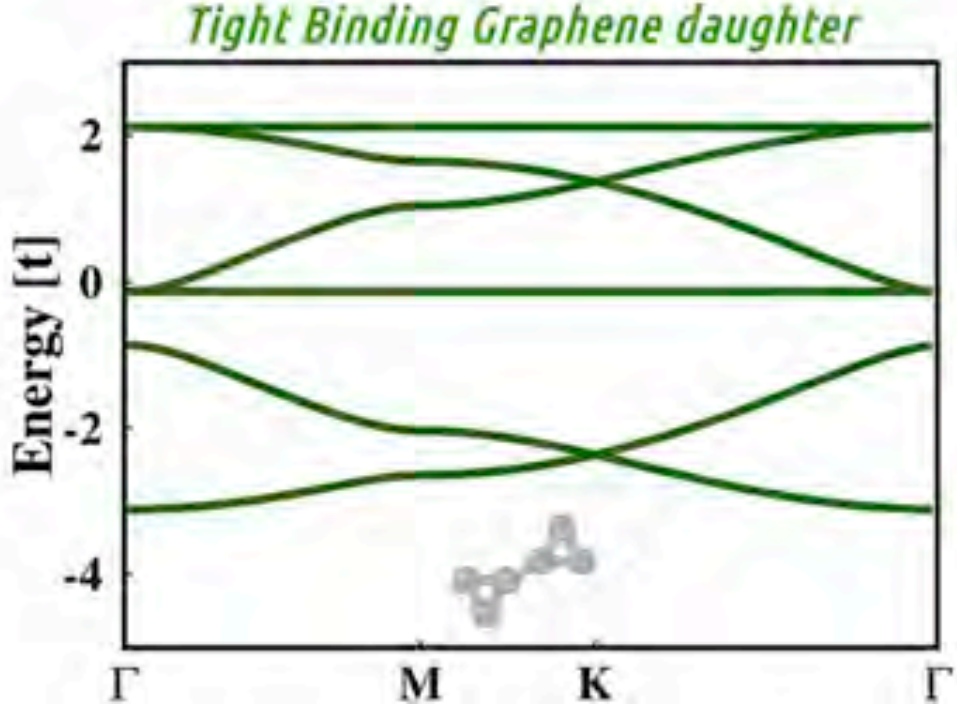
Tight Binding Graphene daughter
Energy [t]
2
0
-2
-4
Γ
M
K
Γ

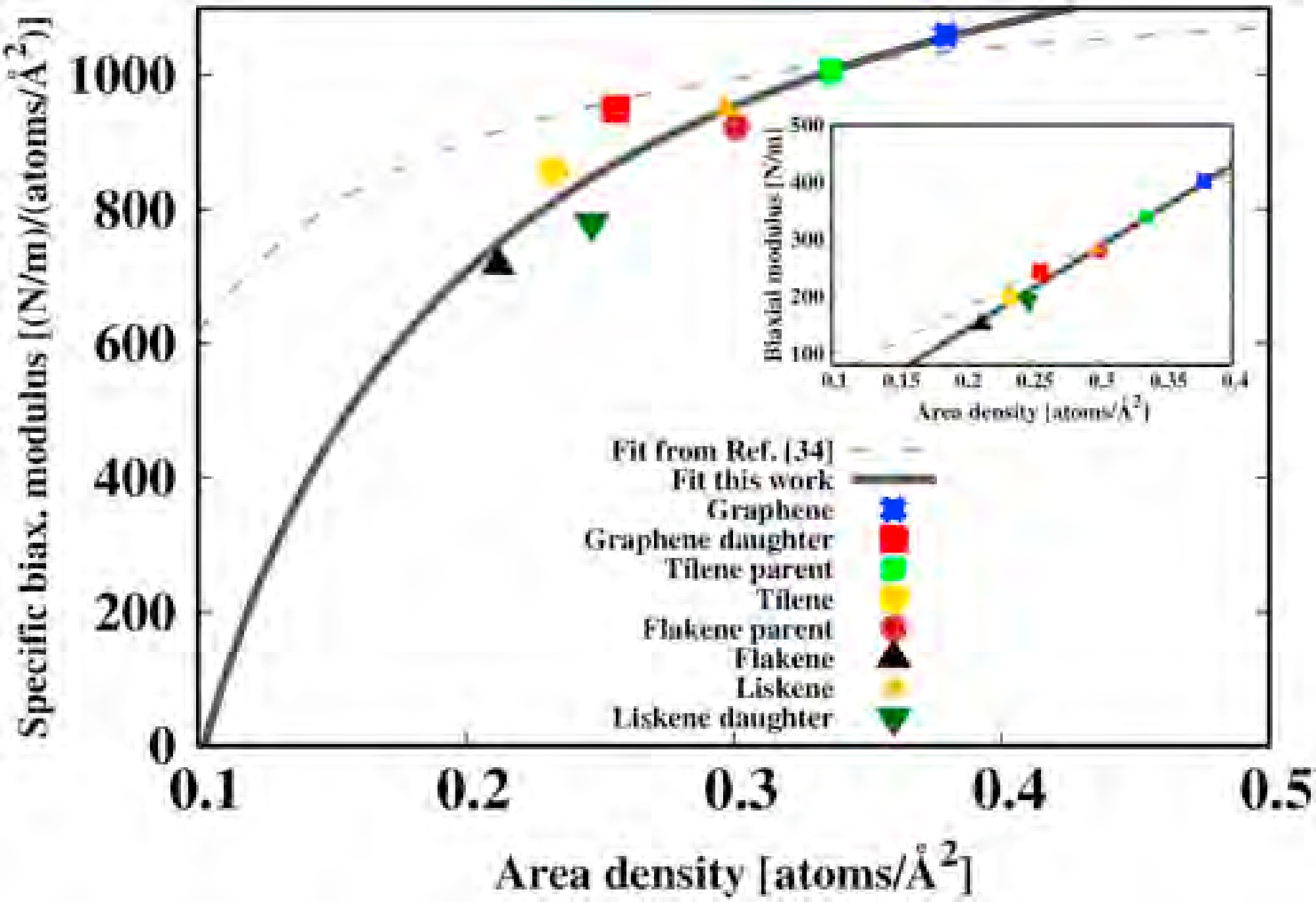
Specific biax. modulus [(N/m)/(atoms/Å^2)]
1000
800
600
400
200
0
0.1
0.2
0.3
0.4
0.5
Area density [atoms/Å^2]
Biaxial modulus [N/m]
500
400
300
200
100
0.1
0.15
0.2
0.25
0.3
0.35
0.4
Area density [atoms/Å^2]
Fit from Ref. [34]
Fit this work
Graphene
Graphene daughter
Tilene parent
Tilene
Flakene parent
Flakene
Liskene
Liskene daughter

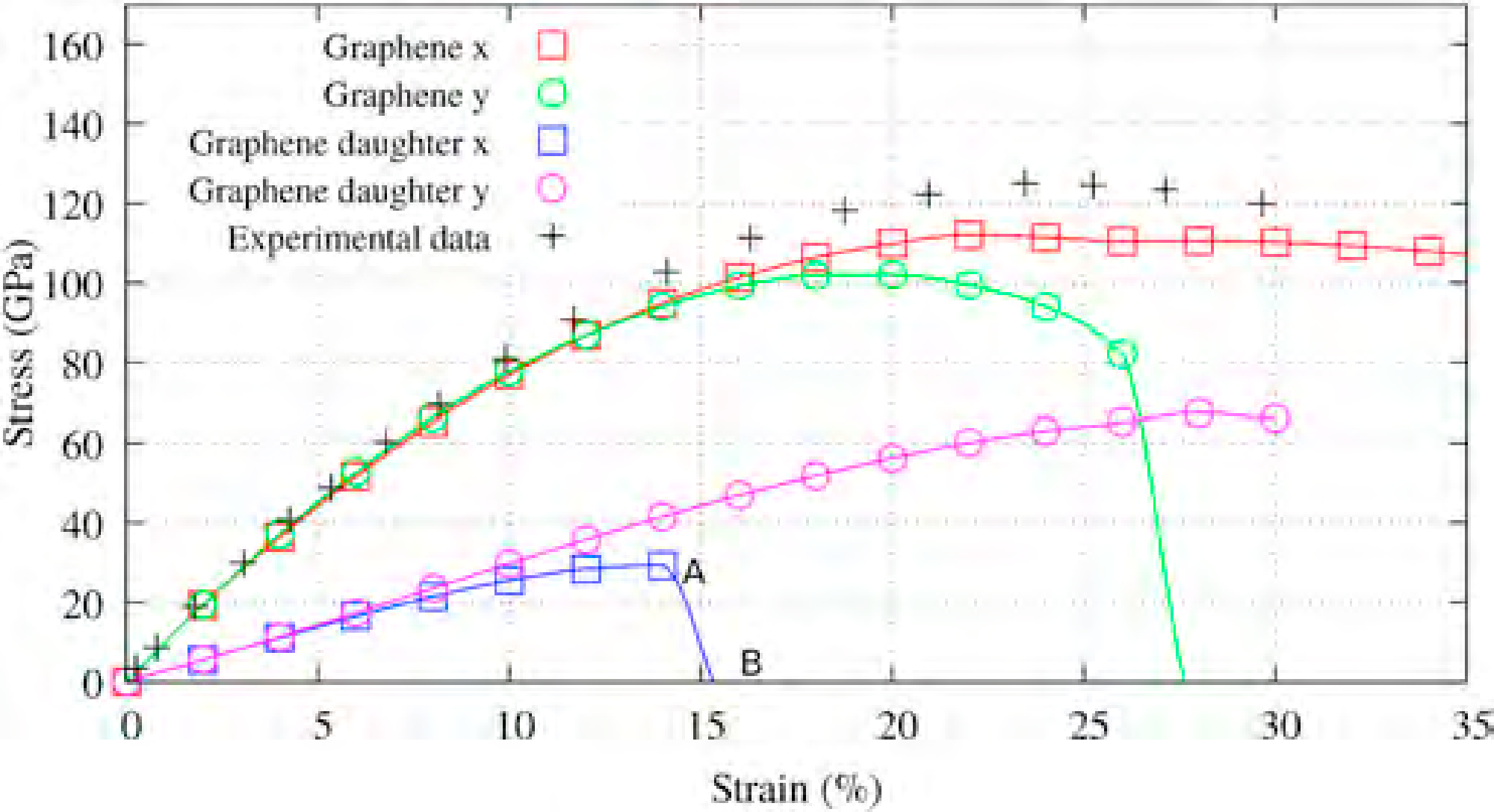
Graphene x
Graphene y
Graphene daughter x
Graphene daughter y
Experimental data
A
B
Stress (GPa)
Strain (%)
0
20
40
60
80
100
120
140
160
0
5
10
15
20
25
30
35

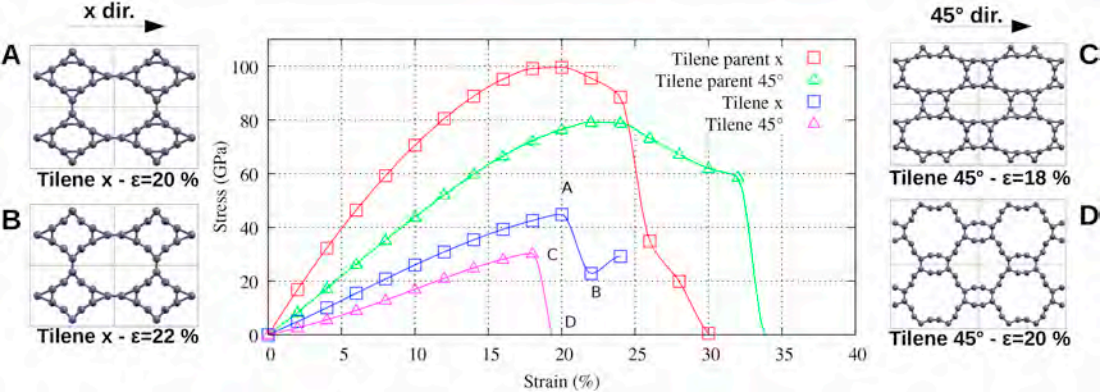
x dir.
45° dir.
A
B
C
D
Tilene x - ε=20 %
Tilene x - ε=22 %
Tilene 45° - ε=18 %
Tilene 45° - ε=20 %
Tilene parent x
Tilene parent 45°
Tilene x
Tilene 45°
Stress (GPa)
Strain (%)
0
20
40
60
80
100
0
5
10
15
20
25
30
35
40

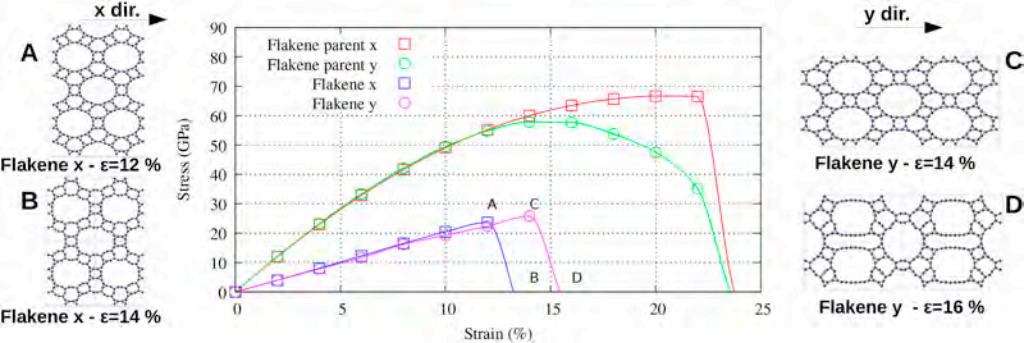
x dir.
A
Flakene x - ε=12 %
B
Flakene x - ε=14 %
Flakene parent x
Flakene parent y
Flakene x
Flakene y
Stress (GPa)
Strain (%)
A
B
C
D
y dir.
C
Flakene y - ε=14 %
D
Flakene y - ε=16 %

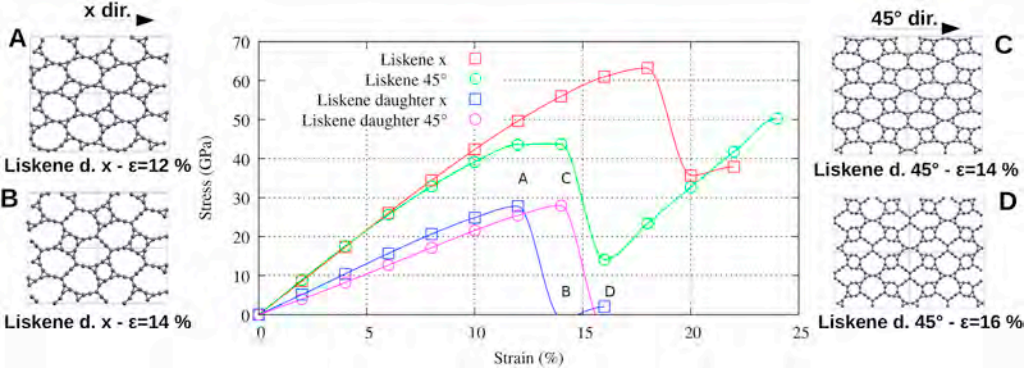
x dir.
A
Liskene d. x - ε=12 %
B
Liskene d. x - ε=14 %
Liskene x
Liskene 45°
Liskene daughter x
Liskene daughter 45°
Stress (GPa)
Strain (%)
A
B
C
D
45° dir.
C
Liskene d. 45° - ε=14 %
D
Liskene d. 45° - ε=16 %